A new setup for fast carbon nanotube growth
rapid thermal control and in-situ monitoring

van Laake, L.C.

Award date:
2006

A New Setup for Fast Carbon Nanotube Growth:
Rapid Thermal Control and in-situ Monitoring

L.C. van Laake

MNSE2006005

Master's thesis

Supervisor: Prof. Dr. A.H. Dietzel
Coaches: Prof. Dr. ir. M.G.D. Geers (substitute Chair of the Committee)
Dr. Y. Bellouard
ir. F.G.A. Homburg

EINDHOVEN UNIVERSITY OF TECHNOLOGY
DEPARTMENT OF MECHANICAL ENGINEERING
MICRO- AND NANO-SCALE ENGINEERING

Eindhoven, May 2006

Preface

In April 2005 I was provided with the opportunity to study at the Massachusetts Institute of Technology in the group of Professor Alex Slocum. His PhD-student John Hart was working on carbon nanotubes, some kind of new material, and was willing to supervise a Master's student from the Netherlands. Little did I know that this was going to be such an intense experience.

Working in a new field was stimulating and challenging, and I hope to have contributed to it a bit; I know I have learned a lot from trying.

I will never forget the fantastic time at MIT and I want to thank all who made it to what it was.

Special thanks to Alex, John, and the rest of PERG. To Andreas and Yves.

Financial support was provided by KIVI, de Schuurman Schimmel-van Outeren Stichting, de Fundatie van de Vrijvrouwe van Renswoude, L&P Group BV, Eindhoven University of Technology, and MIT.

Luuk van Laake

Eindhoven, May 2006

Summary

Carbon nanotubes (CNT) have the special property that their electronic behavior (metallic or semi-conducting) depends on minute changes in their structure. Due to their interesting properties, much interest in CNT has led to a rapid advancement of the field. However, a better understanding of the growth mechanism is needed to develop improved production methods.

A simple setup for rapid heating and cooling based on resistive heating of a silicon element has been developed. Modeling shows that the concept works, and this is experimentally verified. Rapid heating and cooling with at least 40°C/s is possible.

In-situ observation, enabled by the new setup, shows crack-formation in growing nanotube films. This kind of observations was previously impossible because the reaction took place inside a closed tube furnace. Film thickness as a function of time can be observed, and growth rate and ultimate length are improved by separation of the gas (preheating) temperature and the substrate heating. Observations with this new apparatus may lead to better understanding of the kinetics of CNT growth.

A second setup, aimed at locally growing nanotubes by laser heating, has been designed.

Samenvatting (in Dutch)

Koolstof nanobuisjes hebben de bijzondere eigenschap dat ze elektrisch geleidend of half-geleidend zijn afhankelijk van minieme variaties in hun structuur. Onder andere daardoor zijn ze een geliefd studie-object en er is de laatste jaren dan ook veel kennis vergaard in dit veld. Beter begrip van hun groeimechanisme is nodig om tot verbeterde productiemethoden te komen.

Een opstelling voor snelle verhitting en koeling en in-situ observatie is ontwikkeld. Modellering toont aan dat het concept werkt en dit is experimenteel bevestigd. Verhitting en koeling met tenminste 40°C/s is mogelijk.

Experimenten met de nieuwe opstelling laten zien dat er scheuren ontstaan in de groeiende laag nanobuisjes. Dit soort observaties was niet eerder mogelijk, omdat de reactie onzichtbaar in een buisoven plaatsvond. Ook kan de laagdikte eenvoudig optisch gevolgd worden tijdens de groei. Experimenten die mogelijk gemaakt worden met deze manier van verhitting zullen inzicht in het groeimechanisme van nanobuisjes doen toenemen.

Door voorverhitting van koolwaterstoffen in combinatie met verhitting van het substraat, wordt de groeisnelheid en uiteindelijke laagdikte van nanobuisjes verhoogd.

Een tweede opstelling, die groei van koolstof nanobuisjes in laag-vacuum en onder laser verhitting mogelijk moet maken, is ontworpen.

Contents

List of Symbols

Acronyms

CNT	carbon nanotube or carbon nanotubes
CVD	chemical vapor deposition
DC	direct current
HH	half heater
MEMS	micro electro-mechanical system
MWNT	multi-walled (carbon) nanotube
PDE	partial differential equation
PECVD	plasma enhanced chemical vapor deposition
RF	radio frequency
SB	steel block
SEM	scanning electron microscopy
SWNT	single-walled (carbon) nanotube
TEM	transmission electron microscopy
VACNT	vertically aligned carbon nanotubes

Symbols

$\vec{C}$	chiral vector
θ	chiral angle [rad]
e	energy density [J/m^3]
A	cross sectional area [m^2]
ϕ	heat flux [W/m^2]
Q	dissipated power density [W/m^3]
I	current [A]
ρ	resistivity [Ωm]
P	perimeter [m]
w	heat flux to surroundings [W/m^2]
u	temperature [K]
σ	Stefan-Boltzmann constant = 5.67×10^{-8} [W/(K^4 m^2)]
ϱ	mass density [kg/m^3]
k	thermal conductivity [W/(m K)]
$R_{thermal}$	thermal resistance [K/W]
$\tilde{u}$	scaled temperature [–]
$\tilde{x}$	scaled spatial vector x [–]
$\tilde{t}$	scaled time [–]
τ	time constant [s]
V	volume [m^3]
R	thermal resistance [K/W]
Fo	Fourier number [–]
$\tilde{Q}$	scaled power density [–]
$\tilde{R}$	scaled thermal resistance [–]
Nu	Nusselt number [–]
h	convection heat transfer coefficient [W/(m^2 K)]
Ra	Rayleigh number [–]
Re	Reynolds number [–]
T	temperature [K]
w	beam radius [m]
θ_{FF}	far field divergence half-angle [rad]
z_R	Rayleigh range [m]
M^2	correction factor for non-sphericity of Gaussian beam [–]
λ	wavelength [m]
f	focal distance [m]

Chapter 1

Introduction

The field of carbon nanotubes (CNT) is relatively new, but it has advanced at a very high pace because of the enormous research effort that has been and still is invested in this topic. Fifteen years after their discovery in 1991 a large body of literature and knowledge has developed, but some fundamental questions remain unanswered. E.g. the growth mechanism of CNT is not fully understood, and most likely the optimum method of synthesis is yet to be discovered. A more thorough understanding of the growth kinetics could lead to more insight in growth initiation, growth termination, the relation between reaction conditions and quality and type of CNT, and eventually to better production methods.

Thermal CVD is widely used to synthesize substrate-bound CNT, most commonly in a tube furnace which heats both the reaction gases and the substrate. The use of a regular tube furnace has some disadvantages:

- Its large thermal mass inhibits rapid continuous temperature control.
- Substrate temperature is closely coupled to the gas temperature and is not directly monitored, but rather assumed to be equal to the temperature measured by a thermocouple close to but outside the tube.
- In situ growth characterization is difficult to implement in a CVD reactor [Zhu05].

Studies involving rapid heating and thermal cycling have shown that, like temperature itself, temporal temperature variation can be a significant parameter in catalytic reactions. E.g. a 40% increase in conversion rate of the oxidation of CO was reported under forced temperature oscillations [Han06], and formation of SWNT occurred only under rapid heating [Li04].

In situ monitoring of CNT growth rates would be helpful to optimize the CNT growth process and explore the mechanisms and kinetics of CNT growth [Lou03].

It is concluded that an alternative setups enabling rapid thermal control and possibly in-situ monitoring could open up interesting new research opportunities.

This thesis describes work done on two related projects: at the Massachusetts Institute of Technology (MIT) with PhD-candidate John Hart in the Precision Engineering Research Group of Prof. Alexander Slocum, and at Eindhoven University of Technology with Dr. Yves Bellouard in the section Micro- and Nano-Scale Engineering of Prof. Andreas Dietzel. Both projects focus on thermal control and in-situ monitoring for studies of carbon nanotube growth.

Hart's work at MIT is focussing on growth of carbon nanotubes in micro-channel devices, to study the effect of reactant flow velocity on growth. Such micro-scale devices have large surface to volume ratio, low thermal mass, and thus rapid thermal response, making them very suitable for studies of (rapid) temperature variation.

Bellouard and Dietzel proposed a reaction chamber based on laser heating, for in-situ studies of CNT growth.

1.1 Objective

The **overall objective** of this work is to enable rapid thermal control and in-situ monitoring in studies of carbon nanotubes.

The **objective of the first project** is to design a furnace apparatus that enables rapid heating and cooling of substrates for studies of CNT growth.

- More specifically, in stead of a plain substrate the mentioned micro-channel devices should be accommodated, as well.

The **goal of the second project** is to design a vacuum setup for studies of CNT growth, based on back-side laser heating of silicon samples.

- The proposed configuration comprises a CO_2-laser focused on a catalytic layer deposited on the top surface of a silicon substrate. The laser beam enters from the bottom side, rendering the top surface (where the reaction takes place) open for in-situ observation.

1.2 Approach

Chapter 2 gives an introduction to carbon nanotubes to put the designs in some context: history, structure and properties, and synthesis are briefly discussed.

Design and analysis of the furnace apparatus are described in Chapter 3. Choice of the heating principle and thermal modeling lead to the final design. A prototype and improved version of the apparatus are produced and tested.

Experimental results are reported in Chapter 4.

In Chapter 5 the design of the vacuum setup is presented. The setup is produced, but has not been tested yet.

Finally, in Chapter 6 conclusions and recommendations are given and future experiments are proposed.

Chapter 2

Introduction to CNT

Carbon nanotubes were discovered by Iijima in 1991. He found tubular structures of carbon atoms consisting of several concentric cylindrical walls, when investigating by transmission electron microscopy (TEM) the needle-like structures produced on the negative carbon electrode in an arc discharge evaporation process [Iij91]. This structure is referred to as a multi-walled nanotube (MWNT). He was thus the first to image the individual walls of a CNT, revealing the atomic structure that we now understand to cause their special properties.

However, he was probably *not* the first one to synthesize CNTs: Although there are no high resolution images to support the assumption, Baker in the 1970's [Bak72, Bak75] and even before 1900 [Hug89] describe process conditions where CNTs may have formed, and the reported results, if not prove, at least do not contradict CNT formation. Baker even describes a growth mechanism for the apparently hollow thin filaments he finds, which is still considered accurate for CNTs today.

Furthermore, in the 1980's the occasional occurrence of very small diameter carbon filaments during carbon fiber production was reported [Iij80, Obe76a, Obe76b], but no detailed systematic studies were carried out until after 1985, when Kroto et al. published the discovery of Buckminster fullerene: a spherical C_{60} molecule, commonly known as "buckyball", that consists of 60 C-atoms arranged like the patches on a soccer ball [Kro85]. This discovery prompted the systematic investigation of carbon filaments of very small diameter, and Smalley[1] and others speculated that a single-walled nanotube (SWNT) with a diameter comparable to a buckyball (≈ 0.7nm) might be a limiting case of fullerenes. These then still hypothetical molecules were predicted to exhibit unique electronic behavior.

Iijima's images bridged the gap between theoretic speculation and experimental observation of CNT. After his publication, research effort increased rapidly and theoretical predictions of the optical and electronic properties of CNTs started to develop

---

[1] Richard Smalley (June 6, 1943 October 28, 2005), Robert Curl, and Harold Kroto jointly received the 1996 Nobel Prize in Chemistry for the discovery of fullerenes

[Sai92, Ham92, Min92]. Only two years later, in 1993, SWNT were first synthesized by Iijima [Iij93], and at the same time by Betune [Bet93]. [Dre01, Mey05]

Since 1991, thousands of articles have been published on CNT properties, synthesis and applications, a Google-search on "carbon nanotubes" now gives approximately 3.5 million hits, and SWNT are sold for prices as high as $150 per gram. Clearly, there is much interest in this material. But what are these special properties of CNT that make them so fascinating, and how are they produced? These questions are addressed in the current chapter.

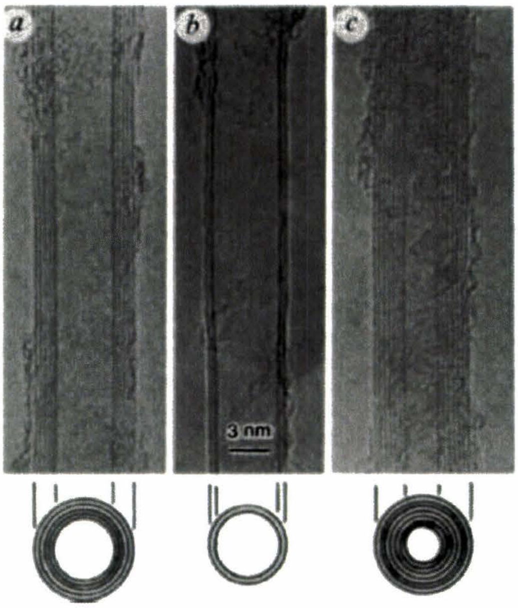

(a) MWNT (Iijima, Nature 1991)

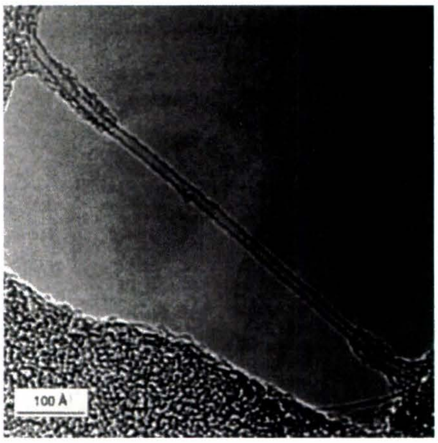

(b) SWNT (Bethune, Nature 1993)

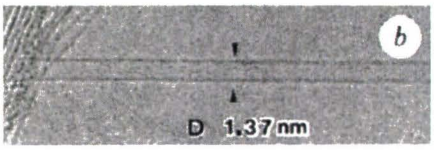

(c) SWNT (Iijima, Nature 1993)

Figure 2.1: First published images of CNT

2.1 Structure and properties

An ideal CNT is a cylindrical, hollow carbon structure that consists of a single shell (SWNT) or multiple concentric shells (MWNT) one atom thick. Each shell can best be imagined as a sheet of carbon atoms arranged in a honeycomb pattern, that is rolled up to a cylinder (although CNT are not necessarily formed by such a mechanism). These honeycomb sheets are called graphene and they are the same layers that, when stacked up, form the well known ideal crystal structure of graphite shown in Fig. 2.1

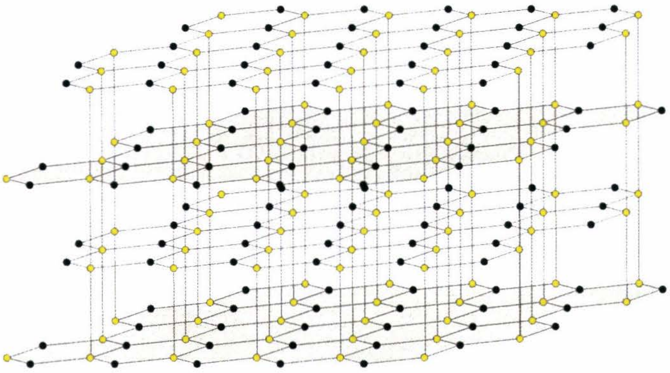

Figure 2.2: Ideal crystal structure of graphite

In perfect graphite the 2D layers are stacked in an alternating fashion, so that of six atoms in a hexagon, three are aligned with an atom in the adjacent layers, and three are over the center of a hexagon in the adjacent layers (Bernal 'ABAB' stacking). The graphene sheets are very strong in-plane, while they are bound together by weak van der Waals forces. Actual graphite often contains staking errors, decreasing the interaction among layers. With enough faults present there is no correlation between the position of the atoms in adjacent layers. This structure is called turbostratic graphite and these 2D turbostratic graphene layers are essentially what CNT shells are made of.

Graphene[2] has a special electronic structure that is between semiconductor and metal: a semiconductor with zero bandgap, or equivalently a metal with zero density of states at the Fermi level. The difference between a large sheet of ideal graphene and nanotubes arises from the periodic boundary condition in the circumferential direction. In fact, similar electronic effects are observed in sub micrometer-scale width pieces of graphite of a few atomic layers (< 5) thickness [Ber04, Nov04].

2.1.1 SWNT

The exact electronic properties of SWNT depend on the orientation of hexagons with respect to the tube axis. Nanotubes of different diameter and "chirality" result depending on the way the sheet is rolled. This is illustrated in Fig. 2.3(a), where the chiral vector $\vec{C}$ and chiral angle θ are defined in terms of the unit vectors $\vec{a}_1$ and $\vec{a}_2$ as $\mathbf{C} = n\mathbf{a}_1 + m\mathbf{a}_2$. The sheet is rolled up such that $\vec{C}$ is around the perimeter of the resulting tube (point A falls on point O). It can be seen that infinitely many ways of rolling are possible (assuming there is no bound on the diameter), some resulting in equivalent structures due to the symmetry in the honeycomb. Therefore, the chiral angle is limited to $0° \leq \theta \leq 30°$ measured with respect to the first lattice vector $\vec{a}_1$.

---

[2] Isolated graphene sheet is not an allotrope of carbon, it has other elements around its edge. It exists as a building block of graphite (stacked) or as a nanotube (rolled)

Chiral angles of $\theta = 0°$, $\theta = 30°$, and $0° < \theta < 30°$ result in zigzag, armchair, and chiral nanotubes, respectively (Figs. 2.3(b) – 2.3(d)).

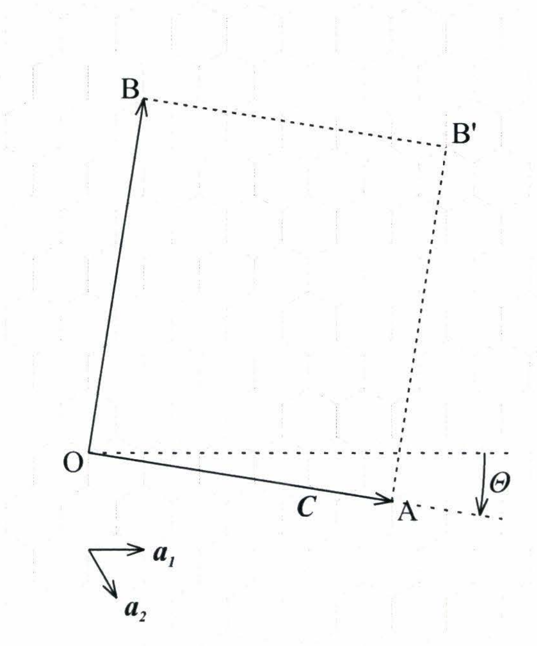

(a) Graphene

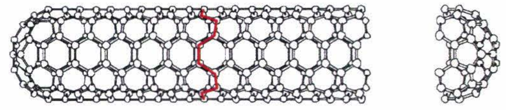

(b) Armchair SWNT, corresponding to $\theta = 30°$

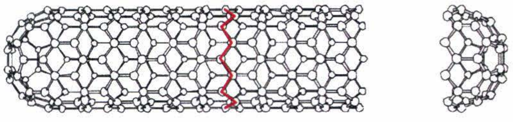

(c) Zig-zag SWNT, corresponding to $\theta = 0°$

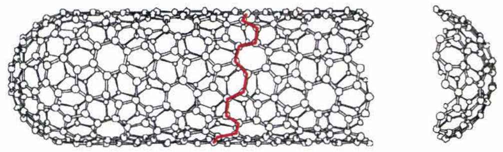

(d) Chiral SWNT, corresponding to $0° < \theta < 30°$

Figure 2.3: ideal SWNT structures (adapted from [Dre01])

Whether CNT are metallic or semiconducting follows from a simple rule: CNT with $n = m$ are metallic (so all armchair tubes are metallic). CNT with $n - m = 3k$, k integer, are semiconducting with a tiny bandgap. This bandgap arises from the curvature of the tube, and decreases with temperature and diameter, so that at room temperature these tubes are also metallic for practical purposes. Other tubes are semiconducting, with bandgap decreasing with diameter.

2.1.2 MWNT

A multi-walled nanotube is a collection of coaxial single-walled nanotubes with increasing diameter. Typically, the electronic properties are less rich then those of SWNT. Bandgap decreases with diameter, and most MWNT are metallic. However, MWNT are very useful as electrically conducting material.

2.1.3 other properties

Not only electrical properties of CNT are fascinating, thermal conductivity higher than diamond, high thermal stability, mechanical strength and stiffness, combined with flexibility make CNT an interesting material for numerous applications.

2.2 Fabrication methods

Under certain conditions gaseous carbon solidifies in the form of carbon nanotubes. Three widely known and used methods are arc discharge, laser ablation, and chemical vapor deposition.

2.2.1 Arc discharge

The first observed MWNT [Iij91] were formed in an arc discharge process. Soon after, improved arc growth methods for production of large quantities were reported [Ebb92]. The general process is based on the vaporization of carbon from one electrode and deposition on another in the form af CNT. Fig. 2.2.1 illustrates the process.

A DC-arc is generated between two graphite electrodes separated by a gap of a few millimeters and held in an inert atmosphere of He at subatmospheric pressure. The anode (+) is consumed in the process and a deposit forms on the cathode (−). The deposit has a hard outer shell and soft fibrous core, that partially consists of CNT.

For the production of SWNT, a composite anode of graphite and a transition metal like Ni or Co is used [Iij93, Bet93]. Carbon then deposits on the reactor surfaces: on the chamber walls, and as a web suspended between cathode and walls.

The arc discharge method produces CNT that generally have very little defects, which is attributed to the high temperature in the arc, but the deposit contains less than 50wt% CNT and has to be purified after production. [Mey05]

2.2.2 Laser ablation

Like the arc discharge method, laser ablation produces high quality CNT. A laser pulse is focussed on a graphite target in an atmosphere of carrier gas (commonly Ar at subatmospheric pressure) inside a tube that may be heated to $\approx$ 1200 K in a furnace. The target locally reaches an extremely high temperature ($\approx$ 6000K) and the vaporized carbon forms CNT-containing soot that is collected on a cooled collector located downstream in the furnace.

If a small amount of metal is added to the target SWNT form, whereas a pure carbon target results in MWNT.

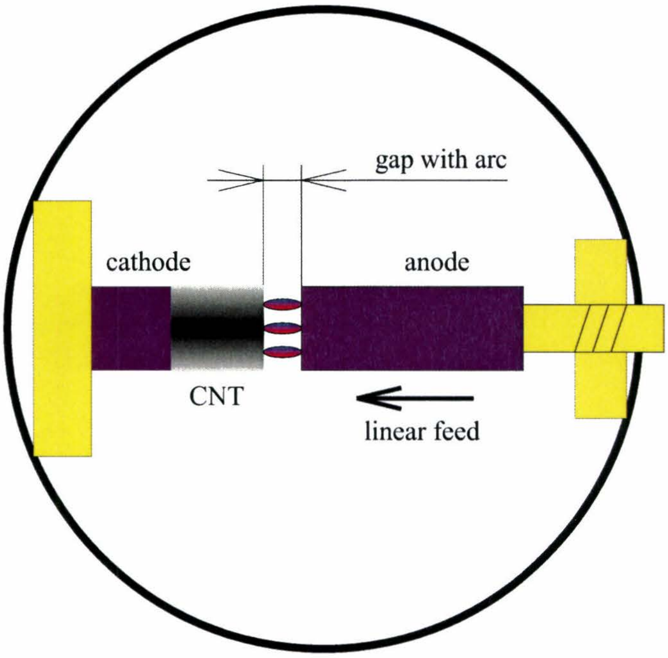

Figure 2.4: Arc discharge

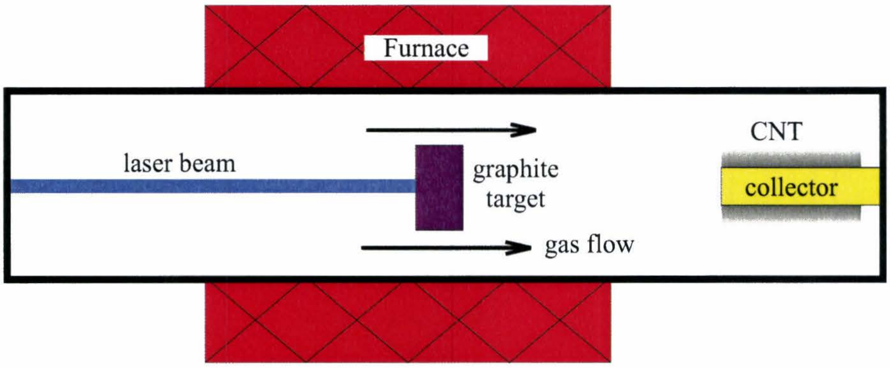

Figure 2.5: Laser ablation

2.2.3 Chemical vapor deposition

Chemical vapor deposition is increasingly used to grow CNT. In the CVD process, a carbon rich gas dissociates at a catalyst particle and the carbon precipitates from the catalyst as a nanotube. For the carbon feedstock carbon monoxide (CO), methane (CH_4), ethylene (C_2H_4), and acetylene (C_2H_2) are often used. The two most common types of CVD are thermal CVD (often simply called CVD), and plasma enhanced CVD (PECVD). In thermal CVD the heat is supplied by a traditional heat source, most often a tube furnace. In PECVD, energy for dissociation of the carbon feedstock comes from the plasma, and lower temperature growth has been reported.

Compared to arc discharge and laser ablation methods, CVD gives much better control over the shape and structure of the product. Mats of tangled nanotubes, vertically aligned nanotubes (VACNT), or individual nanotubes on a specific location can be produced by appropriate choice of catalyst and reaction conditions, e.g. the catalyst layer can be patterned by high accuracy micro-machining techniques to produce mats of nanotubes of arbitrarily shaped footprint. High purity CNT can be produced, but may have more defects than those produced by arc discharge and laser ablation methods.

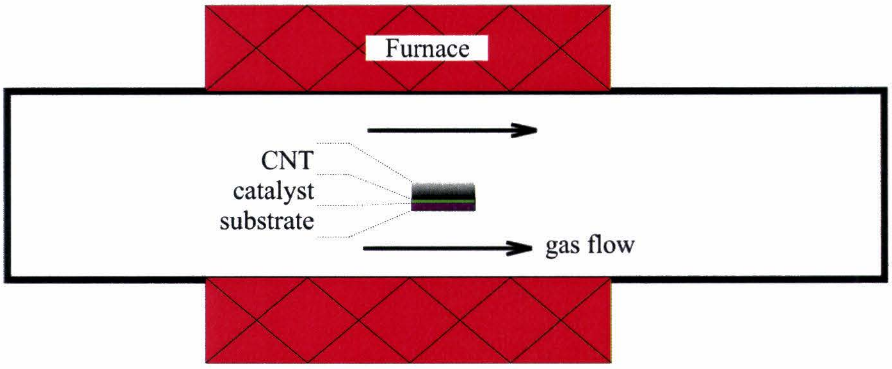

Figure 2.6: Thermal chemical vapor deposition

Chapter 3

Resistively heated substrate design

In this chapter the design of a furnace apparatus based on resistive heating of a silicon heater element is presented. Its purpose is to enable rapid heating and cooling of substrates for studies of CNT growth, and in particular of a micro-channel device designed by John Hart [Har05a].

At present, most growth experiments are conducted without the use of the micro-channel device, but rather on regular substrates. Not only is the operation of the device in the current tube-furnace setup somewhat cumbersome, but experiments of regular substrate bound reactions show fascinating results that can later be applied when using the micro-channels. Therefore both regular substrate and micro-channel experiments are to be performed with the new apparatus.

First, the existing micro-channel device and general setup are described. Then, design objectives are stated, and a new setup is proposed. Dynamic thermal behavior of the system is simulated and a physical setup is produced and tested.

3.1 Existing setup

The existing setup for **micro-channel experiments** consists of four main elements: (1) micro-fabricated silicon reactor device, (2) quartz fixture, (3) standard single zone tube furnace and (4) gas handling system.

1. The key element of the reactor is an array of *parallel micro-channels*, or more accurately grooves, etched in a silicon chip (48 channels on 34 × 19mm, Fig. 3.1(a)). The channels are divided in an entry region and a reaction region (Fig. 3.1(b)) where the entry region is the dominant flow restriction. The growth regions

are all equal, and the variation in entry region dimensions results in flow velocities varying between 0.001 m/s and 1.0 m/s on the same chip. Because of the parallel architecture parametric studies can be performed ceteris paribus.

2. Sealed channels are formed by clamping the micro-channel device against a substrate with a (patterned) catalytic layer, inside a *quartz fixture*. The package is force-closed by ceramic bolts preloading inconel washers.

3. This assembly is placed inside a 42mm quartz *tube furnace* for operation. Reactant gases are delivered to the channels through quartz tubes connected to the package, or are alternatively drawn in from the atmosphere of the tube furnace by an underpressure on the exhaust side.

4. High purity *gases* are delivered from cylinders close to the setup. Pressure regulators on the cylinders maintain a constant pressure and the flow is controlled by rotameters and a mass flow controller. Gases join at a manifold and are delivered to the setup via high purity compatible hosing. On the exhaust side a bubbler provides a slight back-pressure, or in case of the drawing-in mode, pressurized nitrogen powers an underpressure generator.

Fig. 3.1(c) shows the setup. A typical experiment takes ≈90 minutes: in Appendix A.1 the protocol is summarized.

In the micro-channel setup some alignment of CNT with gas flow has been shown in the high-flow channels (John Hart, unpublished results). Other experiments include shape replication of the micro-channels to a film of aligned CNT and studies

For **regular substrate experiments**, a typical run takes ≈80 minutes: the protocol is summarized in Appendix A.2.

Using this setup, many effects are studied and equally many parameters are found to influence results. Some examples are growth under different flow-alternating configurations, variation of the catalyst pretreatment time, and variation of local areal catalyst density.

Flow is alternated by placing a nitride-covered substrate directly on ("capped"), or suspended over ("shielded") the growth substrate, spaced by 2.5 mm, where normally the growth substrate is uncovered ("open"). This causes a transition between local growth of tall and aligned pillars in the "open" case, dense and tall aligned CNT around the edge, decreasing in length towards the middle in the "capped" configuration, and tall aligned growth on the entire substrate when "shielded".

Pretreatment with H_2/Ar changes the activity of the catalyst particles, and it is found that the duration of pretreatment is critical. Growth improves considerably when increasing the duration from 0 to 5 minutes, but for 15 minutes of pretreatment, hardly any growth occurs.

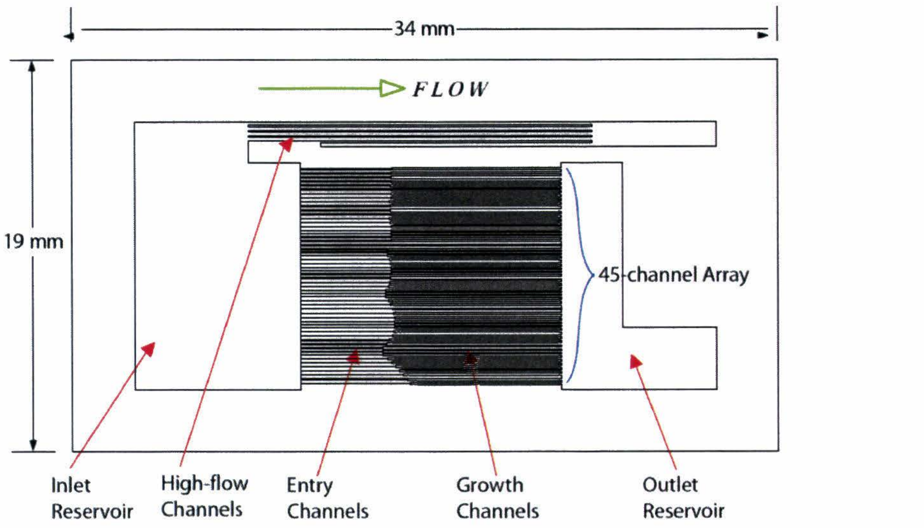

(a) Dimensions and layout

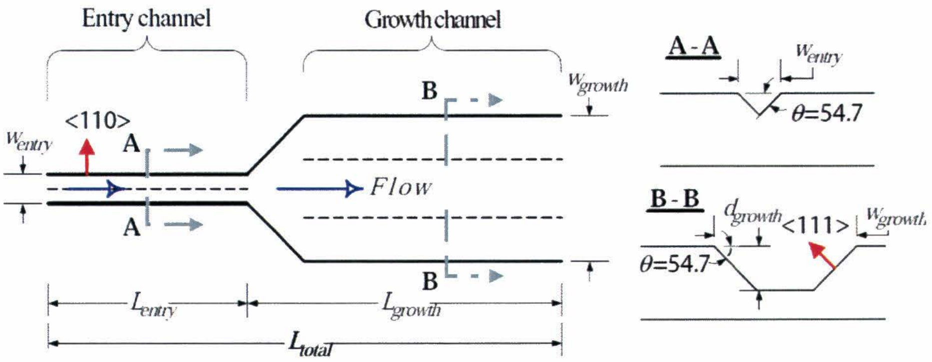

(b) Growth channel and entry region

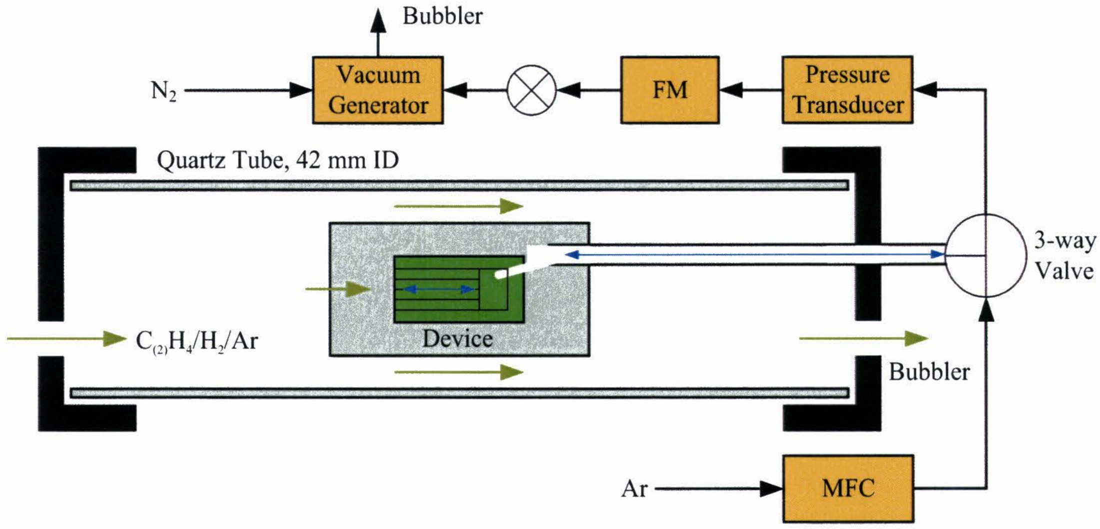

(c) Micro-channel device in tube furnace setup

Figure 3.1: Micro-channel device and operation

Local areal catalyst density is studied on substrates with patterned catalyst layers. Features as small as a few micrometers across may catalyze aligned growth, although smaller features are more prone to bending than bigger (e.g. $> 20\mu$m) ones. But not only do size and shape matter, nearby features also influence growth: pillars grown from identical catalyst patches on the same substrate in the same run differ in length between virtually no growth and 250 μm depending on the distance to other nearby catalyst patches, and this effect is stronger with increasing partial pressure of Ar.

These brief results serve to show that CNT growth is very sensitive to many parameters, that some parameters are coupled, and that possibly many more effects remain to be discovered, even with regular substrates. The micro-channel device on the other hand is specifically useful for combinatorial studies, studies of flow velocity, and has a possible application for fabrication of long CNT strands [Har05b, Har05c, Har06].

3.2 Design objectives

Stating requirements for experimental equipment may sometimes seem a "strange loop"[1], since the physics that determine the optimum configuration is exactly what is to be studied using the equipment.

However, some time scales concerning CNT formation are known, for example:

- Rapid heating on the order of 1000° C/s, achieved by injecting catalyst into a fluidized-bed reactor, resulted in selectivity towards SWNT. It is hypothesized that smaller catalyst particles form due to the rapid heating [Li04]
- Rapid heating, achieved by quickly moving a quartz tube into the hot zone of a tube furnace (≈900°C), resulted in very long (up to cm-scale) SWNT that are aligned with the gas flow. It is hypothesized that upon moving the tube into the furnace, the substrate is heated faster than the surrounding air, and a resulting convection flow upward from the substrate causes the SWNT to be lifted up into the laminar flow of the furnace, out of the boundary layer that exists close to the substrate [Hua03, Hua04].
- In-situ TEM monitoring of thermal CVD show CNT nucleation and growth by a tip-growth mechanism. Cyclic elongation and contraction of the Ni catalyst particle with a period of ≈ 4 s is observed [Hel04]
- Growth rate of aligned CNT in thermal CVD can be as high as 100 μm/s in the first second (MWNT) [Sue04], or 350 μm/min initially and decreasing exponentially (SWNT) [Fut05].

---

[1] A well known example of a strange loop is the person who locks herself out of her house. She needs the key to get into the house, because the key that will open the door is inside... [Hof79].

- A typical thermal CVD growth time is ≈15 min, after which growth rates decrease and the forming reaction self-terminates.
- Heating rates in a tube furnace are typically around 25°C/min
- The approximate required heating and cooling rates stated a priori by John Hart: heating from 0°C to 1000°C in less than 60 s; cooling with 10 °C/s.

The method used to achieve the highest heating rate of 1000°C/s is not transferable to continuous control substrate-bound thermal CVD. By injecting catalyst in a hot zone, rapid heating may be achieved, but consecutive controlled cooling is impossible, let alone temperature cycling. 1000°C/s is considered as an upper bound on the necessary heating rate, since a distinct effect is reported.

The other method, where rapid heating is obtained by rapidly moving a quartz tube into a tube furnace, also reports a significant rapid heating effect. This method is possibly amenable to rapid cooling or thermal cycling, but is mostly a binary method, where it is difficult to continuous temperature control. A heating rate is not mentioned, but conceivably displacing the tube takes ≈1 s, and consecutive heating is initially dominated by radiation. Assuming $T^4_{furnace} >> T^4_{sample}$, the heating rate can be estimated using a lumped model:

$$M\frac{\mathrm{d}T}{\mathrm{d}t} = \sigma\epsilon A T^4_{furnace}$$

Assuming gray body properties with $\epsilon = 0.5$ for the hot tube furnace wall and the sample with catalyst, temperature of the furnace wall $T_{furnace} \approx 2000$ K, and a thermal mass and surface area of the substrate of $M \approx 0.75$ J/K and $A = 800 \times 10^{-}62$ m^2, the resulting heating rate is ≈ 500°C/s and heating from room temperature to 900 °C/s takes $\Delta T_{heating} \approx 2 + 1 = 3$ s. Thermal mass $M = 0.75$ J/K is estimated for a 20 × 20 × 1 mm silicon sample, using mass density $\varrho = 2.33 \times 10^3$ kg/m^3 and specific heat $C \approx 800$ J/kg K. The temperature of the sample is neglected as $(2000^4 - 900^4) \approx 2000^4$.

Thus, heating rates on the order of 100 - 1000 K/s have in both a very different and a similar system proven to influence CNT growth.

On the other hand, much slower mechanisms also play an important role. The most certain indication is of course the in-situ observation of cyclic events in thermal CVD on a timescale of ≈5 seconds, but the gradual decay of growth rate followed by self-termination happens on an even slower scale of minutes.

What is achievable of course depends on the exact design, but as a starting point the heating rate resulting from effectively heating the micro-channel device with $P = 100$ W of power is coarsely estimated. Assuming the same material properties as before, dimensions of 34 × 19 × 2 mm, and perfect thermal insulation, from a lumped model follows a heating rate of $100/M \approx 100/2.5 = 40$°C/s.

It is concluded that a heating rate on the order of hundreds of degrees per second is almost certain to influence CNT growth, either by altering the catalyst formation, by convection waves, or by another effect. On intermediate scales, e.g. by cyclic heating with a period on the order of minutes, slower effects may be influenced, but this is uncertain. The benchmark tube furnace heats and cools slowly at 25°C/min, but 40°C/s should be achievable from a very coarse estimation for modest power, but super efficiency. This is a 100-fold improvement over the existing situation. Arbitrarily, this value will be used as design objective for heating and cooling. It also satisfies the a priori specified heating rate requirement.

The controllable temperature range is taken between 300°C and 850°C, where 850°C is based on the maximum temperature for CNT growth in the current setup, and 300°C represents the temperature below which CNT are considered not to react with air. Thus, after cooling to that temperature, the furnace apparatus could be opened, but also growth could presumably be stopped completely by cooling to that temperature.

The objective is operationalized as: design and build a simple furnace setup capable of heating and cooling the micro-channel device or smaller regular substrates at a rate of 40°C/s. Temperature has to be controllable on that timescale between 300°C and 850°C.

3.3 Choice of heating principle

Some alternatives for heating principles are presented and compared.

3.3.1 Convection

Above, a heating power $P = 100\text{W}$ was assumed. Let's assume this power is supplied through the surface by convection. The Biot number for this case is $\text{Bi} = \frac{hL}{k}$, with h heat transfer coefficient [W/(m^2 K)], L characteristic length [m] and k thermal conductivity [W/(m K)]. Using L=0.5 mm and $k \approx 100$ W/(m K), $\text{Bi}=5\times10^{-6}\cdot\text{h}$. So $\text{Bi} < 0.1$ for any $h < 2\times10^4$ and the temperature will be approximately constant throughout the substrate, i.e. convection to the substrate dominates conduction in the substrate. From this first approximation, thermal stress should not be a mayor concern, since no large gradients are expected at this Biot number.

To transfer 100 W through one surface $S \approx 500\text{mm}^2$, i.e. a flux of 200 kW/m^2, the heat transfer coefficient has to be $h > fracPS\Delta T \approx \frac{10^6}{\Delta T}$ W/(m^2 K). The temperature of operation is typically 750 - 850 °C, so the fluid temperature should be higher than, say 1000°C, and h results on the order of 10^3 - 10^4. This is a very high value, and gas handling of such high temperature gases, including the alternation between heating and cooling, may be hard to implement.

3.3.2 Radiation

Laser or near-IR heating of silicon is possible depending on the wavelength. At wavelengths above 1 μm, less than 50% of optical power is absorbed, the rest is transmitted and reflected [CIN05]. Below 1 μm efficient heating could be possible. An advantage is that no vibrations are induced, as could be the case by convection heating, and that local heating as well as heating over larger areas is possible.

3.3.3 Electromagnetic induction heating

Electromagnetic induction heating in the microwave and RF range is applicable to rapid heating of silicon wafers [Tho02]. The key challenge in this technique is to get good coupling of the microwaves to the workpiece. From literature, it is apparent that very specialized equipment is needed, capable of producing high frequency, high power output, that is moreover exactly matched to the workpiece, because only then efficient heating takes place. Rapid and volumetric heating is achievable, but the cost and effort to build such a setup is high.

3.3.4 Resistive heating

Indirect resistive heating may be achieved by heating a resistance wire or foil in contact with the substrate. Disadvantage may be that some holder in contact with the substrate slows the thermal response, and the challenge is to make good thermal contact without adding too much thermal mass.

Alternatively the silicon can be resistively heated itself, where the challenge is to make reversible electrical contact to silicon. This is potentially a very simple method, based on volumetric heating.

3.3.5 Selection

Resistive heating of a silicon heater element is selected as the best candidate. Other methods may take much longer to develop, whereas this simple method may be as effective. A silicon heater could be used indirectly, with the substrate placed onto it. Advantages of using silicon over other heater materials are good thermal stability and good thermal contact due to the optical surface finish. Silicon is widely used as substrate material in CNT growth and has proven not to affect the reaction. Alternatively, a silicon sample with catalyst on it can be heated directly. The electrical contact to silicon is the main design challenge.

3.4 Reversible electrical contact to silicon

Electrical contact to silicon is most easily made by depositing a metal (e.g. aluminum) layer and heating to let the metal diffuse into the silicon. This avoids rectifying barrier behavior of the contact, if a metal with appropriate work function is selected [Sze02]. Such bonds may not be stable at high temperature as the metal continues to diffuse into the silicon, and may form a eutectic bond. Doping the silicon with acceptor or donor ions or changing temperature affects the bandgap, and thus the choice of an appropriate metal. By sufficiently doping the silicon or increasing temperature the choice of metals that give good contact is wider.

To obtain the simplest reversible contact, it is preferred to avoid the deposition step and use a clamped contact. If sufficiently doped silicon and an appropriate metal are used, this may be a good solution. Temperature should be low enough to prevent creeping of the clamped contact to maintain the contact force, and to avoid the formation of a permanent eutectic bond, that would result in the destruction of the contact upon opening.

Preliminary tests show that aluminum indeed diffuses into the silicon, and colored streaks are seen to appear in the sample. Upon heating for more than a minute, a eutectic bond forms, resulting in cracking or cleaving of the latter. Stainless steel is found to provide a good solution, having good high temperature properties. A maximum temperature of $\approx 500°C$ is taken to avoid creeping.

3.5 Proposed setup

To obtain a reversible electrical contact it is therefore preferred to keep the contact temperature below 500°C. This solves the aforementioned thermal stability and diffusion issues. Of course, one can imagine actively cooled electrodes, e.g. by means of an impinging air or liquid jet, or a cooling liquid flowing through integrated or external channels. But would it be possible to have passively cooled electrodes, e.g. a thermal mass acting as a heatsink on the contact, of which heat is removed by convection and radiation only? Intuitively one knows that a larger thermal mass in contact with a heated object will heat up less than a small one. But if a large thermal mass is connected to the heater, how are the dynamics changed? In other words: will the substrate still heat up and cool down fast enough?

Fig. 3.5 shows the proposed concept. Both ends of a silicon heater element are clamped between stainless steel blocks that act as self cooling electrodes.

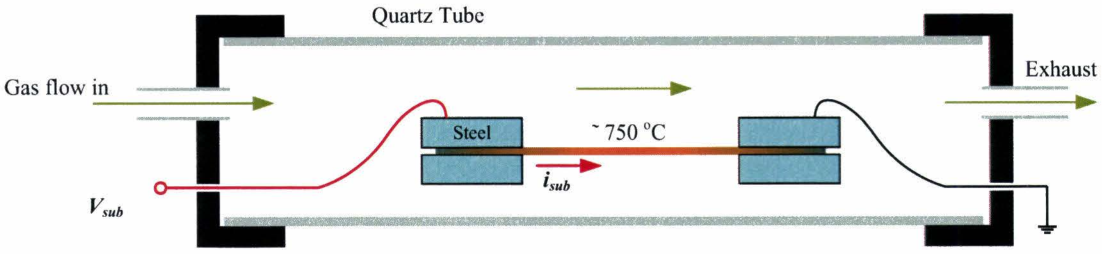

Figure 3.2: Proposed setup: self cooling steel electrodes

3.5.1 Thermal model

An electrothermal model of the concept is written to investigate its thermal behavior (see Fig. 3.3). The following assumptions are made:

1. symmetry around the center: this limits the number of domains to two: Half of the heater (HH), and one steel block (SB).
2. one-dimensionality: no transverse temperature gradients
3. resistivity of steel electrodes negligible
4. literature values for material properties
5. atmosphere remains at constant temperature

The integral form of the energy conservation equation [Hab98] is applied to both domains, resulting in two coupled PDEs. Per domain:

$$\frac{\partial}{\partial t}\int_a^b e(x,t)A\mathrm{d}x = A\Big(\phi(a,t)-\phi(b,t)\Big)+\int_a^b QA\mathrm{d}x-\int_a^b Pw(x,t)\mathrm{d}x \tag{3.1}$$

$$\Leftrightarrow \int_a^b \left(\frac{\partial e}{\partial t}+\frac{\partial \phi}{\partial x}-Q+\frac{P}{A}w\right)\mathrm{d}x = 0$$

$$\Leftrightarrow \frac{\partial e}{\partial t}+\frac{\partial \phi}{\partial x}-Q+\frac{P}{A}w = 0$$

$$\varrho c\frac{\partial u}{\partial t} = \frac{\partial}{\partial x}\left(k\frac{\partial u}{\partial x}\right)+Q-\frac{P}{A}w$$

$$\varrho c\frac{\partial u}{\partial t} = k\frac{\partial^2 u}{\partial x^2}+Q-\frac{P}{A}w \tag{3.2}$$

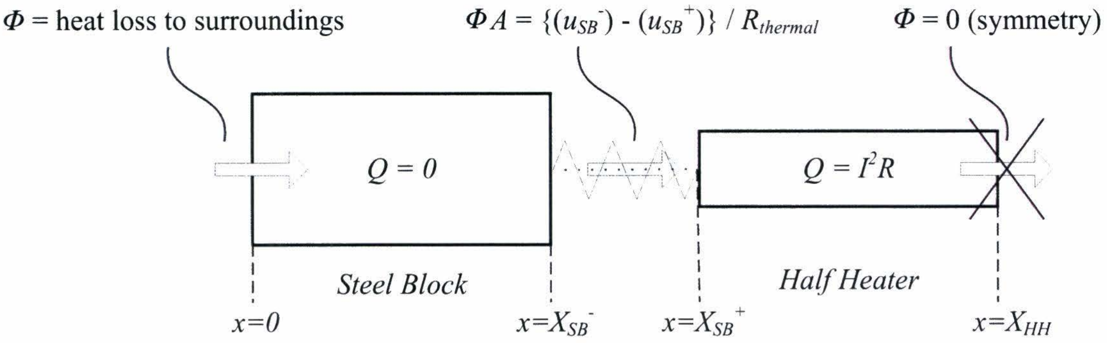

(a) Two domains and boundary conditions

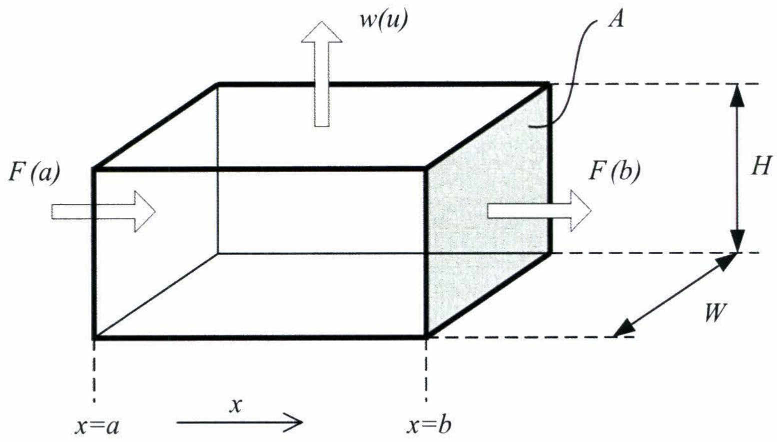

(b) Definition of element for energy conservation

Figure 3.3: Thermal model

Boundary conditions for SB:

$$\begin{aligned} x = 0 &\quad \rightarrow \quad -\phi = h(u - u_\infty) + \sigma\epsilon(u^4 - u_\infty^4) && (3.3)\\ x = X_{SB}^- &\quad \rightarrow \quad \frac{u_{SB}^- - u_{SB}^+}{R_{thermal}} = \phi A_{SB} && (3.4) \end{aligned}$$

Boundary conditions for HH:

$$\begin{aligned} x = X_{SB}^+ &\quad \rightarrow \quad \frac{u_{SB}^- - u_{SB}^+}{R_{thermal}} = \phi A_{HH} && (3.5)\\ x = X_{HH} &\quad \rightarrow \quad \phi = 0 && (3.6) \end{aligned}$$

where Fourier's law of conduction is applied, and

e	energy density [J/m^3]
A	cross sectional area [m^2]
ϕ	heat flux [W/m^2]
Q	dissipated power density $= \frac{I^2\rho}{A^2}$ [W/m^3]
I	current [A]
ρ	resistivity [Ωm]
P	perimeter [m] $P = 2(H + W)$
w	heat flux to surroundings $= h(u - u_\infty) + \sigma\epsilon(u^4 - u_\infty^4)$ [W/m^2]
u	temperature [K]
σ	Stefan-Boltzmann constant = 5.67×10^{-8} [W/(K^4 m^2)]
ϱ	mass density [kg/m^3]
k	thermal conductivity [W/(m K)]
$R_{thermal}$	thermal resistance [K/W]

It is noted that Eqs. 3.1 – 3.2 are valid only for constant cross-section and material parameters. But when solving numerically on a fine grid the integral and differential notations are indistinguishable, because the temperature variation over a small enough distance $\triangle x$ is assumed constant. The differential notation is based on small volumes a priori. The only difference is then the order in which the same assumptions are applied.

Equations 3.2 – 3.6 are made non-dimensional by appropriate scaling, and the defined time constants are calculated for different materials and dimensions. This gives some insight in the effect of the material and size of the electrodes in terms of the temperature of the contacts and the dynamics of the system.

$$\frac{\partial \tilde{u}}{\partial \tilde{t}} = \frac{\tau_o}{\tau_d}\mathrm{Fo}\frac{\partial^2 \tilde{u}}{\partial \tilde{x}^2} - \left(\frac{\tau_o}{\tau_c} + \frac{\tau_o}{\tau_r}\right)\tilde{u} + \tilde{Q} \tag{3.7}$$

Scaled boundary conditions for SB:

$$\tilde{x}_{SB} = 0 \quad \rightarrow \quad \frac{A_{SB}}{S_{SB}}\left(\frac{\tau_o}{\tau_{c,SB}} + \frac{\tau_o}{\tau_{r,SB}}\right)\tilde{u}_{SB} = \frac{\tau_o}{\tau_{d,SB}}\mathrm{Fo}_{SB}\frac{\partial \tilde{u}_{SB}}{\partial \tilde{x}_{SB}} \tag{3.8}$$

$$\tilde{x}_{SB} = 1 \quad \rightarrow \quad \frac{1}{\tilde{R}_{SB}}\left(\tilde{u}_{HH} - \tilde{u}_{SB}\right) = \frac{\tau_o}{\tau_{d,SB}}\frac{\partial \tilde{u}_{SB}}{\partial \tilde{x}_{SB}} \tag{3.9}$$

Scaled boundary conditions for HH:

$$\tilde{x}_{HH} = 0 \quad \rightarrow \quad \frac{\partial \tilde{u}_{HH}}{\partial \tilde{x}_{HH}} = 0 \tag{3.10}$$

$$\tilde{x}_{HH} = 1 \quad \rightarrow \quad \frac{1}{\tilde{R}_{HH}}\left(\tilde{u}_{HH} - \tilde{u}_{SB}\right) = \frac{\tau_o}{\tau_{d,HH}}\frac{\partial \tilde{u}_{HH}}{\partial \tilde{x}_{HH}} \tag{3.11}$$

where

$$\begin{aligned}
\tilde{u}_i &= \frac{u_i - u_\infty}{u_\infty},\ (i = SB, HH) \\
\tilde{x}_i &= \frac{x - x_{min}}{x_{max} - x_{min}} \Rightarrow \tilde{x}_{SB} = \frac{x}{X_{SB}},\ \tilde{x}_{HH} = \frac{X_{HH} - x}{X_{HH} - X_{SB}} \\
\tilde{t} &= \frac{t}{\tau_o} \\
\tau_o &= \tau_{c,HH}//\tau_{r,HH}//\Big(\tau_{d,HH} + \tau_{d,SB} + (\tau_{c,SB}//\tau_{r,SB})\Big)\ |_{u_i=\tilde{u}_i} \\
\tau_{j,i} &= (\varrho C V)_i\, R_{j,i}, \\
V &= (LA)_i,\ L_{SB} = X_{SB},\ L_{HH} = X_{HH} - X_{SB} \\
R_{d,i} &= \left(\frac{L}{kA}\right)_i \Rightarrow \tau_{d,i} = \left(\varrho C V \frac{L}{kA}\right)_i \\
R_{c,i} &= \left(\frac{1}{hS}\right)_i \Rightarrow \tau_{c,i} = \left(\varrho C V \frac{1}{hS}\right)_i \\
R_{r,i} &= \left(\frac{\tilde{u}}{\sigma \epsilon u_\infty^3 S \left((\tilde{u}+1)^4 - 1\right)}\right)_i \Rightarrow \tau_{r,i} = \left(\varrho C V \frac{\tilde{u}}{\sigma \epsilon u_\infty^3 S \left((\tilde{u}+1)^4 - 1\right)}\right)_i \\
\mathrm{Fo}_i &= \left(\frac{k\tau_d}{\varrho C L^2}\right)_i \\
\tilde{Q} &= \frac{Q}{Q^*},\ Q^* = \frac{\varrho C u_i n f}{\tau_0} \\
\tilde{R}_i &= \frac{R_{thermal}}{R_i^*},\ R^* = \left(\frac{L\tau_0}{kA\tau_d}\right)_i
\end{aligned}$$

The scaling of x is clarified in Fig. 3.5.1. $\tilde{x}_{SB}$ and $\tilde{x}_{HH}$ are in opposing directions to improve efficiency in later numerical solving: it is expected that a finer grid will be necessary close to the connection of the two domains, and by this definition the connection is on the same side of scaled space (see also Chapter 3.5.5).

The definition of the scaling factors is not so much intended to generalize the equation or for easier analytical solving, since the temperature-dependent material properties and the radiation term inhibit a simple closed form solution. But the time constants are useful to get a feeling for the thermal behavior even without solving the equation.

It is noted that an elegant solution could be obtained by linearizing around an equilibrium point, removing time-dependent terms by transforming to the Laplace domain, solving, and transforming back to the time domain [Han91]. This is more efficient than time-stepping methods in obtaining temperature profiles at isolated times, but all material dependent properties must be expressed in an analytical function, and when

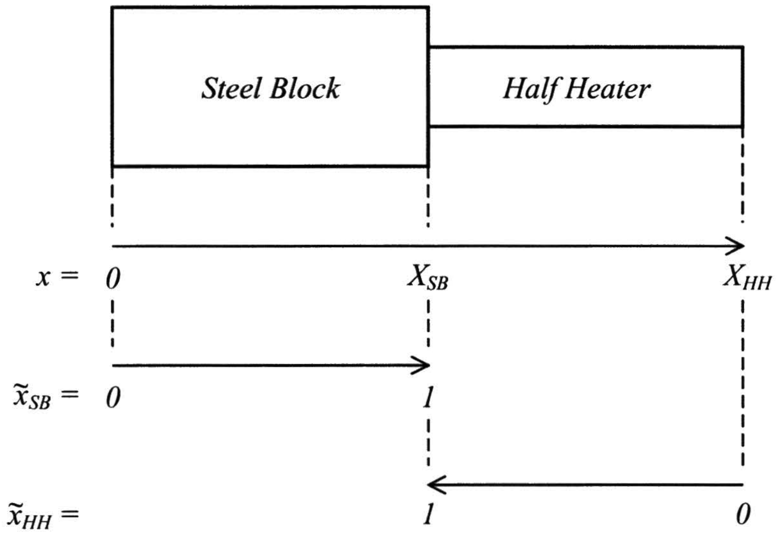

Figure 3.4: Scaling of the spatial variable x

time-varying input (e.g. from measured data) is analyzed, integration over time is unavoidable.

The time *constants* are in fact not constant at all: since the material properties are temperature dependent, so are the defined scaling factors. The term "time constant" should be interpreted as a local (in time) constant. Since the other time constants are implicitly temperature-dependent, there is no objection to writing the time constant for radiation explicitly depending on temperature. The overall time constant is chosen independent of temperature, to ensure synchronization between the two domains while solving.

The physical interpretation of the time constants is especially meaningful for cooling of the silicon element. High heating rates can in principle be achieved by applying a high current, but cooling depends on heat loss. The definition as a product of thermal mass and thermal resistance can be interpreted as "the energy loss needed for a temperature decrease of one degree" divided by the "energy that is lost per second and per degree temperature difference" by a certain mechanism: radiation, convection, or conduction. The result has the units of time: the time it takes to lose the stored energy at the current temperature difference, i.e. the time it takes to cool to the temperature of the surroundings. Without radiation or temperature dependent properties, the time it takes to cool down is independent of temperature, and the typical logarithmic decay results. Of course these are local values, and they don't reveal the whole dynamics.

The overall time constant is defined to represent the physical behavior where heat is lost by convection and radiation, and in parallel by conduction to the steel block (that also loses heat by convection and radiation). It is evaluated at $\bar{u}$, some representative temperature. 400 °C and 700 °C are taken for $\bar{u}_{SB}$ and $\bar{u}_{HH}$.

The physical properties of steel and silicon are treated, after which time constants are calculated as function of temperature.

3.5.2 Material properties

The heater element is cut from a boron-doped silicon wafer. Figure 3.5 shows thermal conductivity and specific heat of silicon as a function of temperature as used in the model [CIN05]. Properties of AISI 304 stainless steel are obtained from [Inc96], and [CIN05] and depicted in Figure 3.6. The temperature dependence is approximated by a least-squares fit for easier numerical solving. The fitting relations and parameters are given by:

Table 3.1: Datafit of thermophysical properties

property	fitted function	A	B	C
$k_{silicon}$	$\mathrm{A}/T^2+\mathrm{B}/T$	5.05×10^6	2.75×10^4	–
$c_{silicon}$	$\mathrm{A}(T+\mathrm{B})^{\mathrm{C}}$	457	-243	0.109
k_{steel}	$\mathrm{A}T^2+\mathrm{B}T+\mathrm{C}$	-2.87×10^6	1.87×10^{-2}	9.58
c_{steel}	$\mathrm{A}T^2+\mathrm{B}T+\mathrm{C}$	-1.59×10^{-4}	0.387	380

The resistivity of doped silicon is a complicated function of temperature, where two mechanisms with opposing effects compete: with increasing temperature, resistivity initially increases, due to increased scattering; it reaches a maximum at the intrinsic temperature; and decreases rapidly at even higher temperatures due to thermally generated electron-hole pairs. In other words: the number of available carriers increases with temperature, while their mobility decreases. The relation between carrier density, mobility and resistivity is simple:

$$\rho = \frac{1}{q\left(p\mu_h + n\mu_e\right)} \tag{3.12}$$

where

q	charge of an electron = 1.6×10^{-19} [C]
p, n	hole resp. electron density [cm^{-3}]
μ_h, mu_e	mobility of holes resp. electrons [cm^2/(V s)]

Measurements of resistivity as a function of temperature of doped silicon were first published by Pearson and Bardeen in 1949 [Pea49a, Pea49b], and later by Morin and Maita [Mor54]. Many theoretical discourses have been published since, but most of them are

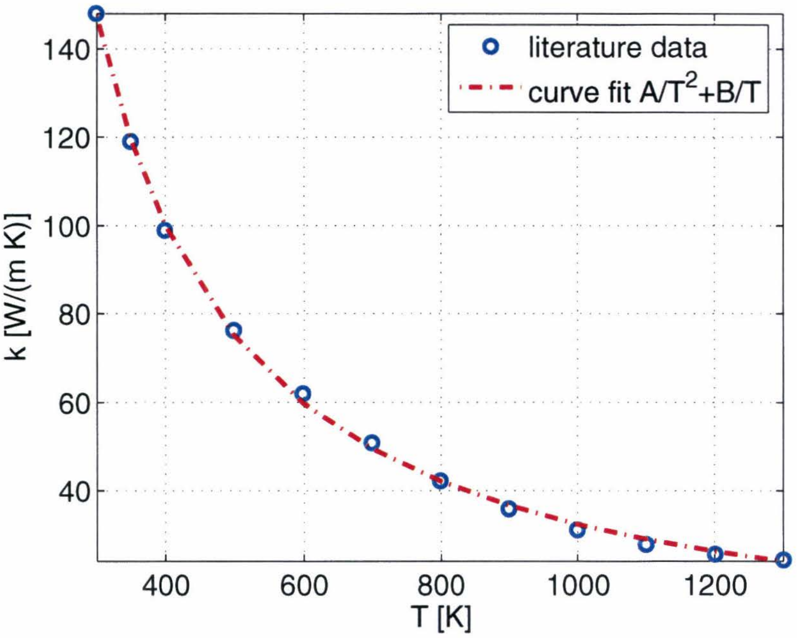

(a) Silicon thermal conductivity

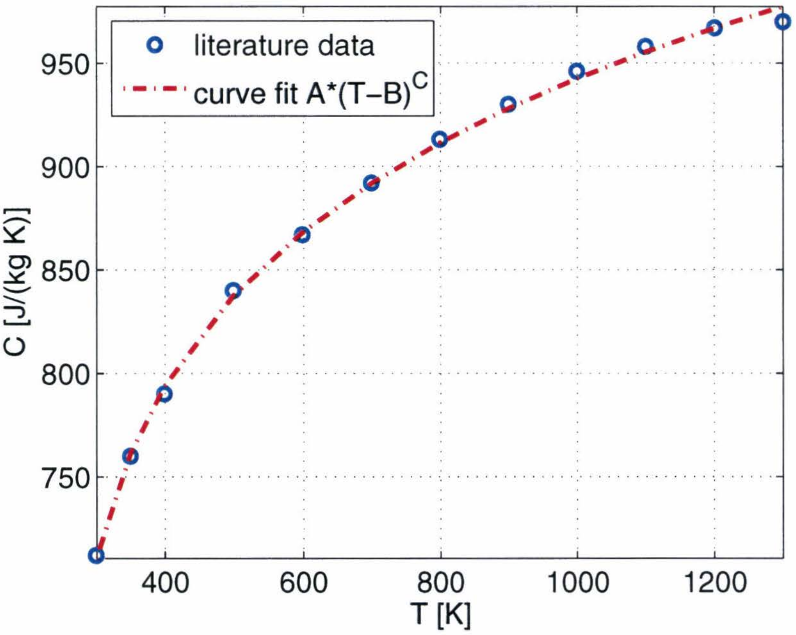

(b) Silicon specific heat

Figure 3.5: Thermophysical properties. Silicon, $N_A = 10^{19}\text{cm}^{-3}$

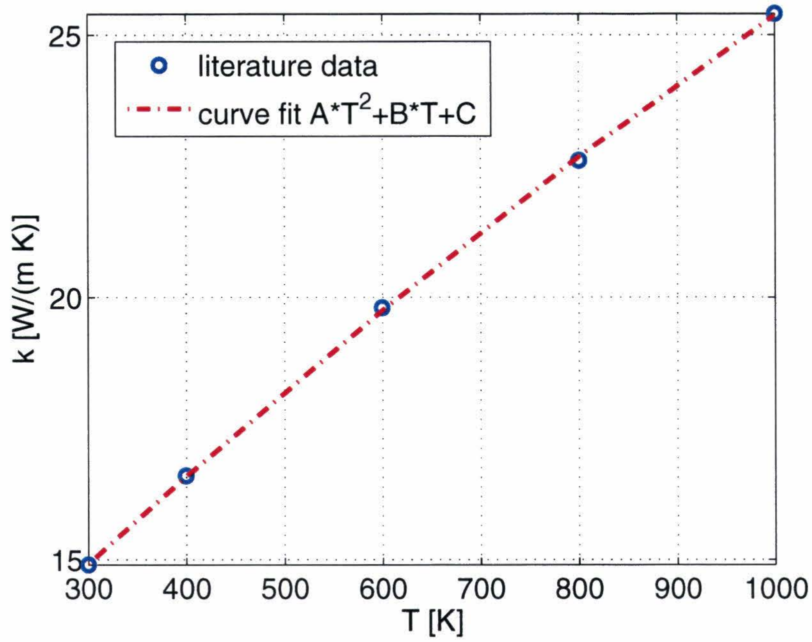

(a) 304 steel thermal conductivity

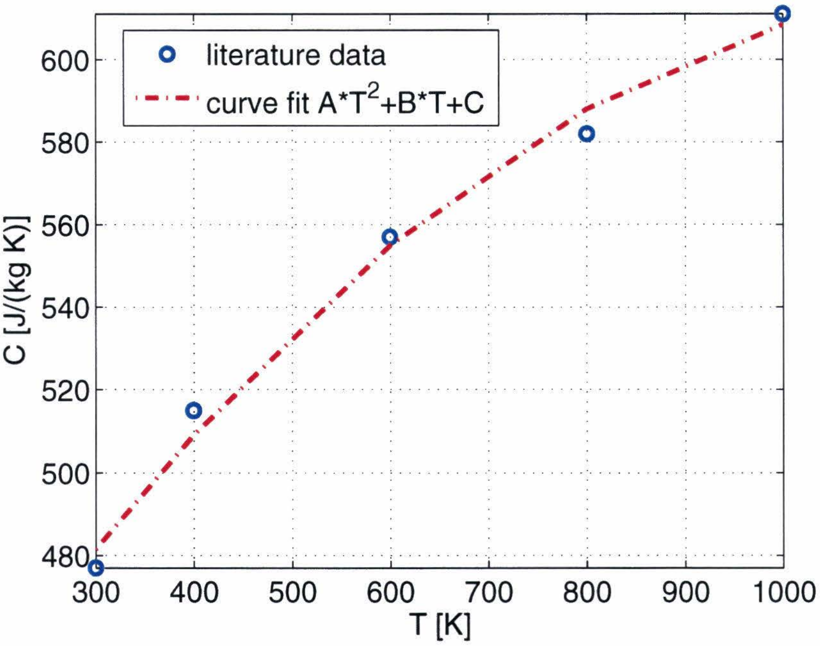

(b) 304 steel specific heat

Figure 3.6: Thermophysical properties. Stainless steel AISI 304

not focusing on high temperatures, as this regime is not interesting for electronics design (unless maybe for failure analysis) because the semiconducting behavior essentially vanishes.

For the model, $\rho(T)$ is obtained by interpolating between the measured values from Pearson and Bardeen, as depicted in Fig. 3.7.

Emissivity, or more accurately total hemispherical emissivity, of both silicon and steel depend on doping, surface finish, and temperature. In fact, values between 0.2 and 0.9 are reported for polished and sandblasted AISI 304 steel, respectively. For now, constant average values of 0.65 for the silicon heater and 0.5 for the steel block are used. They are later verified by infrared measurement.

Mass density of silicon and steel are 2.33×10^3 kg/m^3 and 8.0×10^3 kg/m^3, respectively.

3.5.3 Convection heat transfer coefficient

To estimate the convection heat transfer coefficient the widely used approximations for forced and natural convection over a horizontal plate are compared. The respective Nusselt relations are: ([Jan00])

Heated plate, facing upward (natural convection)

$$Nu = \frac{hL}{k_f} = 0.54\mathrm{Ra}^{1/4},\ 2.6\times10^4 < \mathrm{Ra} < 3\times10^7 \tag{3.13}$$

Heated plate, facing downward (natural convection)

$$Nu = 0.27\mathrm{Ra}^{1/4},\ 3\times10^5 < \mathrm{Ra} < 3\times10^10 \tag{3.14}$$

Heated plate (forced convection)

$$Nu = 0.664\mathrm{Pr}^{1/2}\mathrm{Re}^{1/2},\ Re < 5\times10^5 \tag{3.15}$$

where the symbols are defined as usual and the average values are meant.

The resulting values for h are depicted in Fig. C.1 as function of surface temperature. The calculation and the used fluid properties for Ar are also shown in Appendix C.

The convection coefficients predicted by the forced convection approximation are much lower than the values resulting from the natural convection assumption. Natural convection is concluded to be dominant, which is easily explained from the very low fluid velocity in the tube. The gas flow is less than 1 liter per minute in a tube with diameter $D \approx 50$ mm, resulting in an average gas velocity of $v = \frac{0.001}{\pi(0.025)^2 60} < 0.01$ m/s.

The value for h used in the model for both the steel blocks and the heater element is depicted in Fig. 3.8

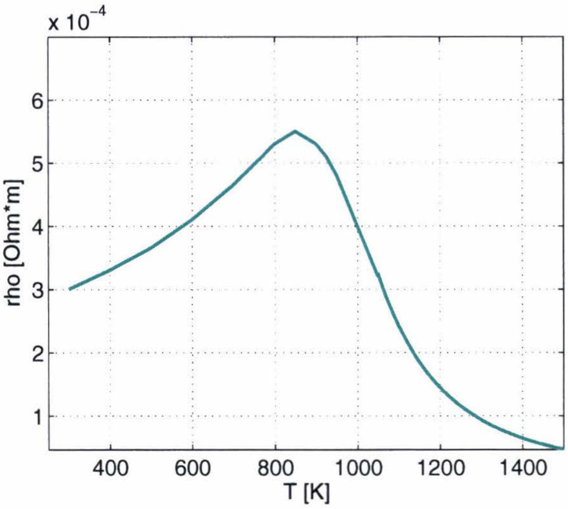

(a) Silicon resistivity

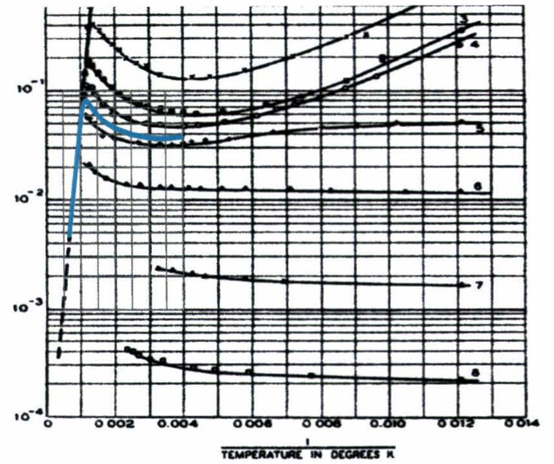

(b) Resistivity, overlaid on original figure by Pearson and Bardeen [Pea49a]

Figure 3.7: Material properties. Silicon, $N_A = 10^{19}\text{cm}^{-3}$

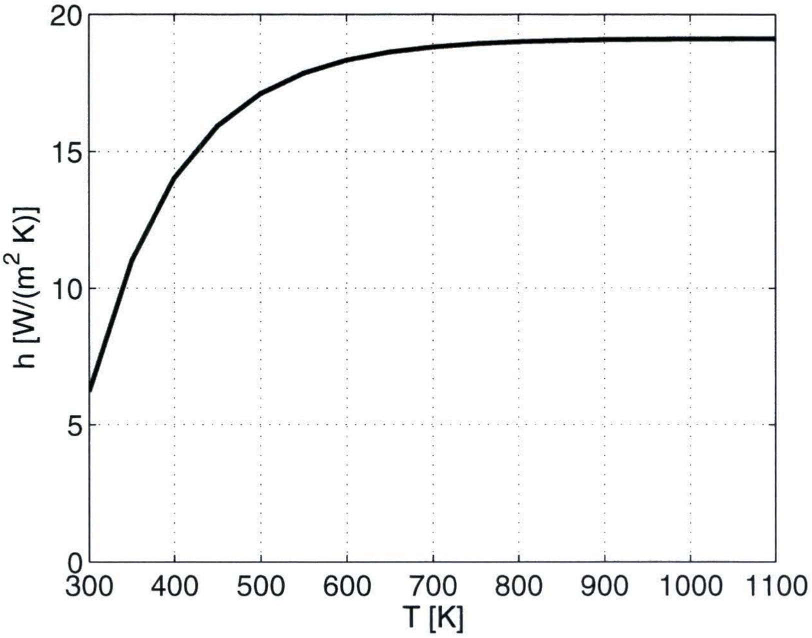

Figure 3.8: Convection heat transfer coefficient used in model

3.5.4 Time constants

With the physical properties known, the time constants are calculated to get a feeling for the cooling rates that can be achieved. The dimensions are taken corresponding to an actual heater that has been tested: each steel block is taken 20 × 10 × 40 mm, and half the heater 10 × 0.3 × 42.5 mm. Fig. 3.9 shows the time constants as function of temperature.

As can be expected, values for the steel block are much higher than for the heater element, and the overall constant is dominated by the silicon.

3.5.5 Simulation results

The model is then numerically solved for given current values, to determine the actual time-domain behavior. The implementation of the thermal model is given in Appendices B and B.2. A block input for the current gives heat-up and cool-down dynamics. A stepwise increase is used to predict temperature, temperature profile, and voltage as function of input current. The results are depicted in the graphs below.

The continuous input power is $P \approx 150$ W at 800°C, corresponding to a voltage of less than $V \approx 40$ V.

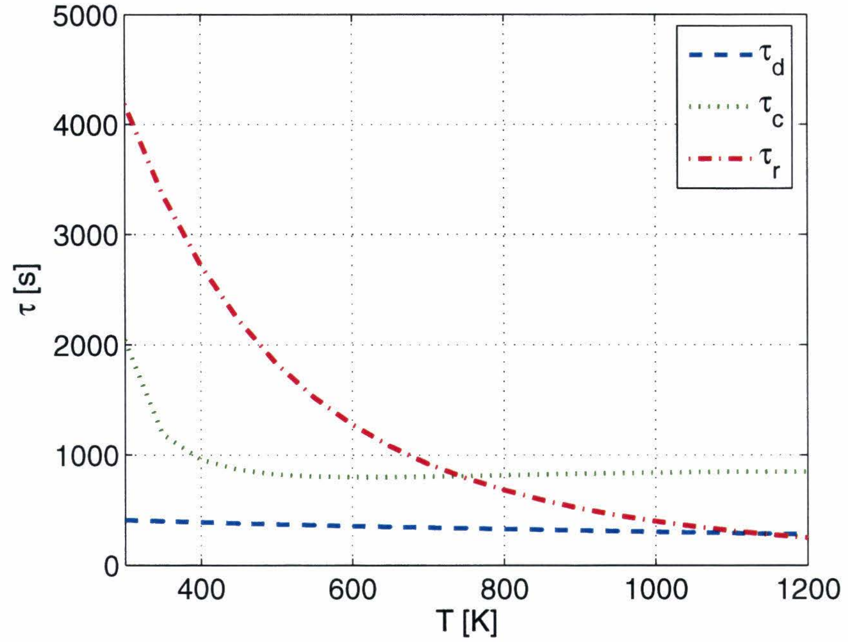

(a) Steel block, 20 × 10 × 40 mm

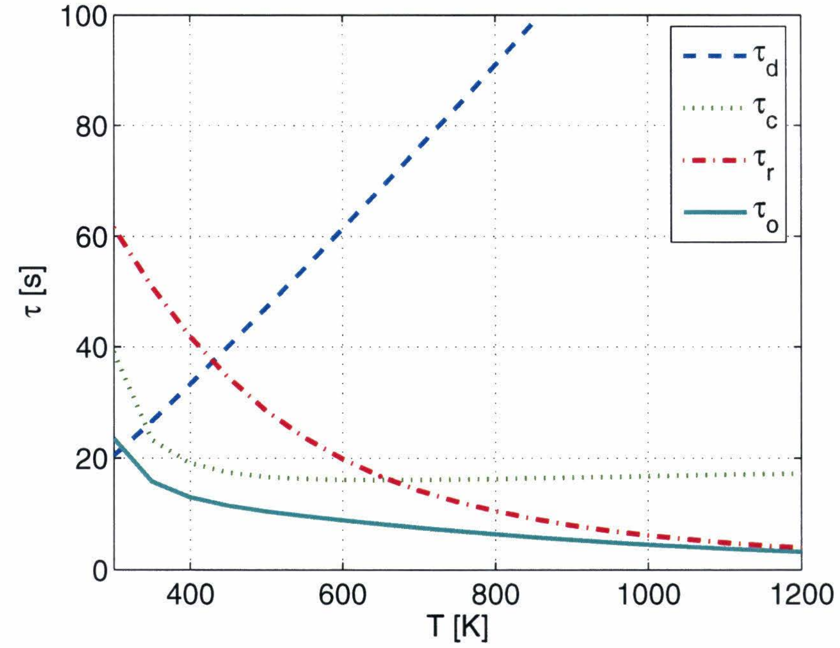

(b) Half heater, 10 × 0.3 × 42.5 mm, and overall time coefficient τ_o

Figure 3.9: Time constants as function of temperature

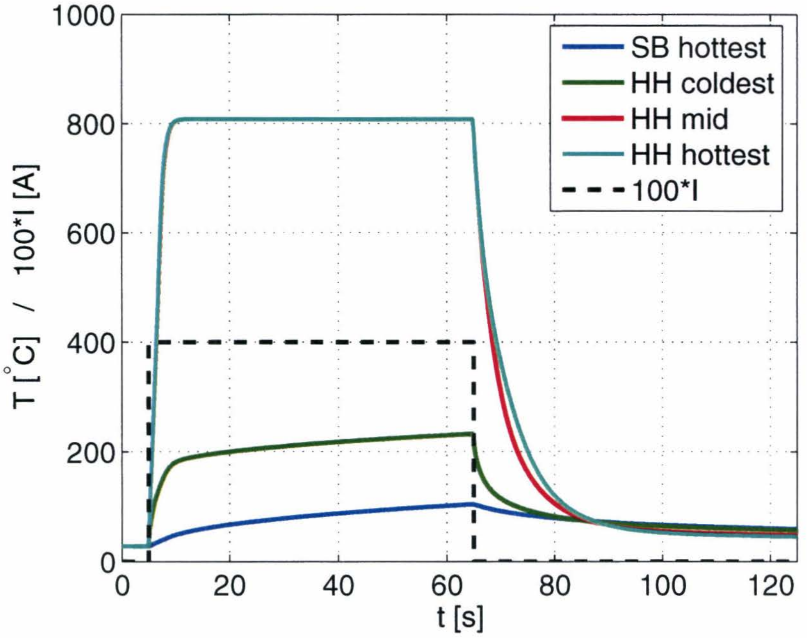

(a) Simulated temperature of selected notes

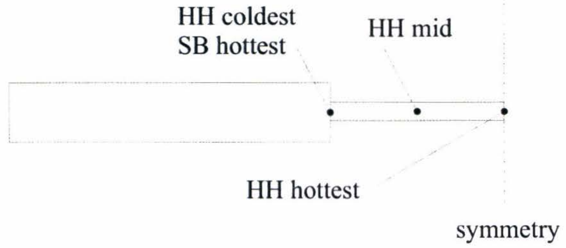

(b) Graphic of the location of the nodes of Fig. 3.10(a)

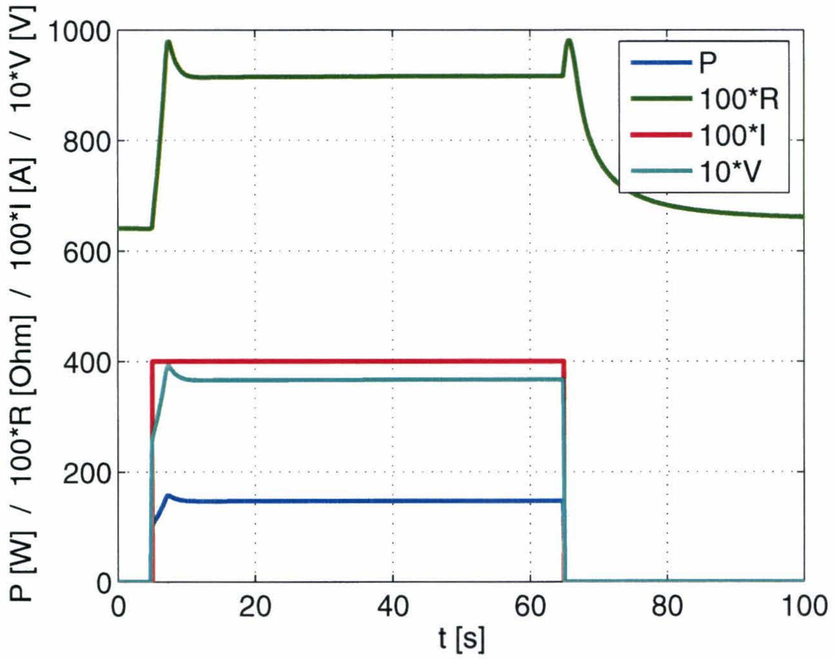

(c) Simulated power, voltage, and resistance for the given input current

Figure 3.10: Simulated response of proposed system to 4 A block current

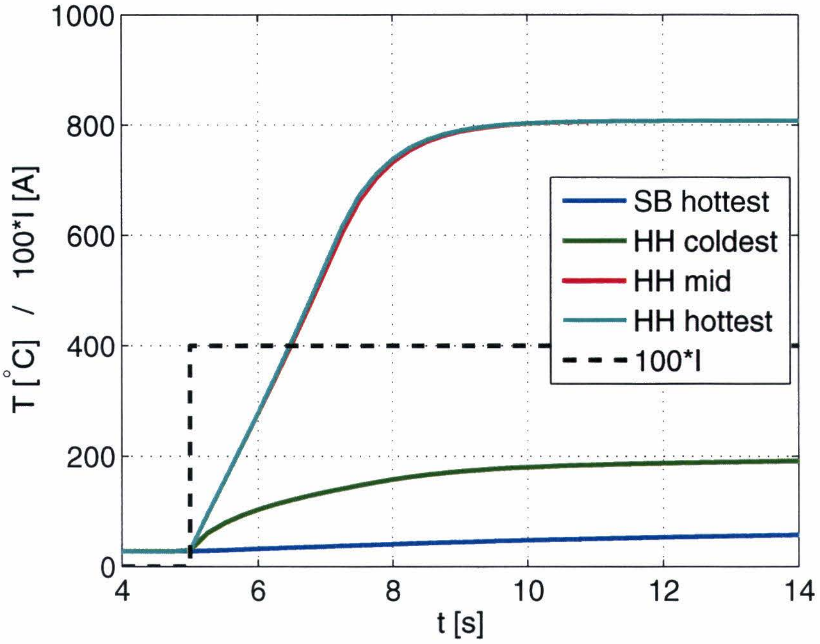

(a) Heating

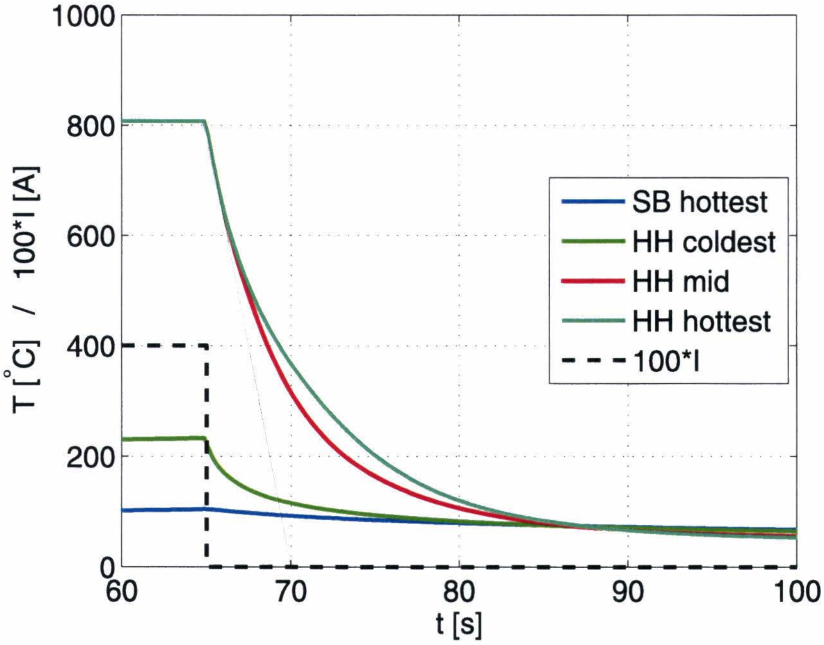

(b) Cooling

Figure 3.11: Response of proposed system to 4 A block current: zoom on heating and cooling

The nodes in Fig. 3.10(a) correspond to the nodes of SB and HH that are in contact (resp. SB hottest and HH coldest), to the last node of HH, i.e. the center of the actual heater element (HH hottest), and a node between HH hottest and HH coldest (HH mid). This is illustrated in Fig. 3.10(b).

Heating from room temperature to 800°C takes ≈5 s. Cooling down from 800°C to 300°C takes less than ≈10 s. The hand-drawn line in Fig. 3.11(b) represents the initial cooling rate, corresponding to a local time constant of ≈5 s, as predicted by the above analysis (See Fig. 3.9(b)).

From Fig. 3.12(b) it is evident that the power doesn't increase linearly with current. This is due to the resistivity of silicon showing a strong decrease at high temperatures (see Fig. 3.7(a)): by increasing the current, temperature increases, resistivity decreases and ever less power is generated per Ampère of current with increasing temperature. This may lead to a clear maximum attainable temperature where any increase in current is canceled by a decrease in resistivity as shown by Bayt [Bay99]. He uses this fact to operate a propulsion heater at very stable temperature. For this geometry and current, this limit behavior is not found, and very high temperatures can be obtained.

This also leads to a flattening of the temperature profile, as shown in Fig. 3.13, where temperature profile is plotted as function of time. The is profile is quite constant over the heater element, and increasingly so with increasing temperature. This is due again to the fact that resistivity decreases with temperature, so less power is dissipated where temperature is highest. This effect is basically a naturally occurring feedback mechanism, simply due to a material property (resistivity decreasing with temperature).

It is noted that if resistivity would increase with temperature, or alternatively if a voltage-source, rather than a current source was used, thermal runaway could occur. In either of those cases, dissipated power would increase with temperature. This *positive* feedback mechanism could lead to dangerous failure by melting of the heater element.

In Fig. 3.12(c) by quasi-static is meant the value 100 s after a step increase.

3.5.6 Experimental verification

The model is also applied to measured values of $I(t)$ and temperature and voltage are compared. The here reported measurement is conducted in the new setup, to be described in the following sections 3.6 and further, because in this new setup it is much easier to instrument a heater element with multiple thermocouples. Several measurements have been conducted with only one thermocouple in the quartz tube setup, also on par with the model.

Fig. ??hows a photograph of the substrate equipped with five thermocouples. Only four are read during the measurement, because of the 6 available channels, two channels were used to log current and voltage. The sample rate is 2 per second. The thermocouples are k-type (chromel-alumel, Omega) with a 75 μm butt-welded junction. To ensure

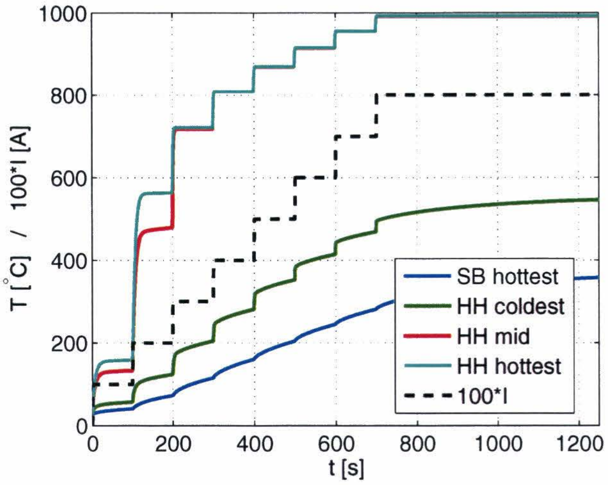

(a) step-increase current: simulated temperatures of nodes as depicted in 3.10(b)

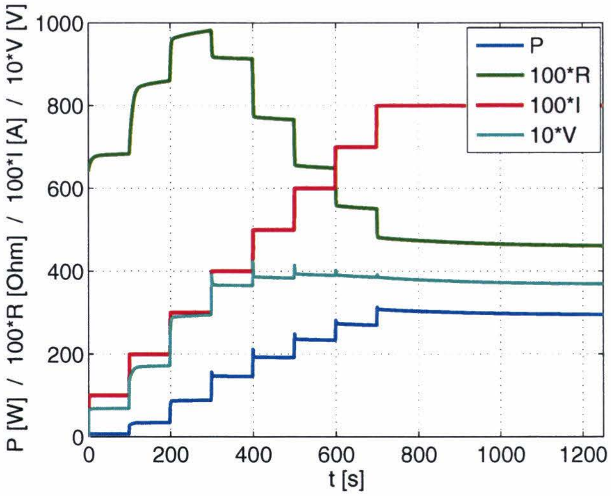

(b) Simulated resistance and power as function of time

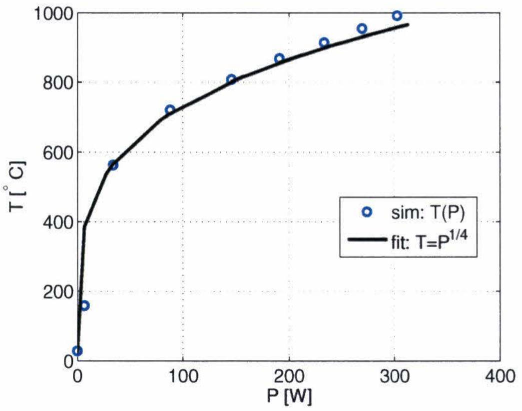

(c) Simulated quasi-static temperature as function of power

Figure 3.12: Response of proposed system to step-increase current

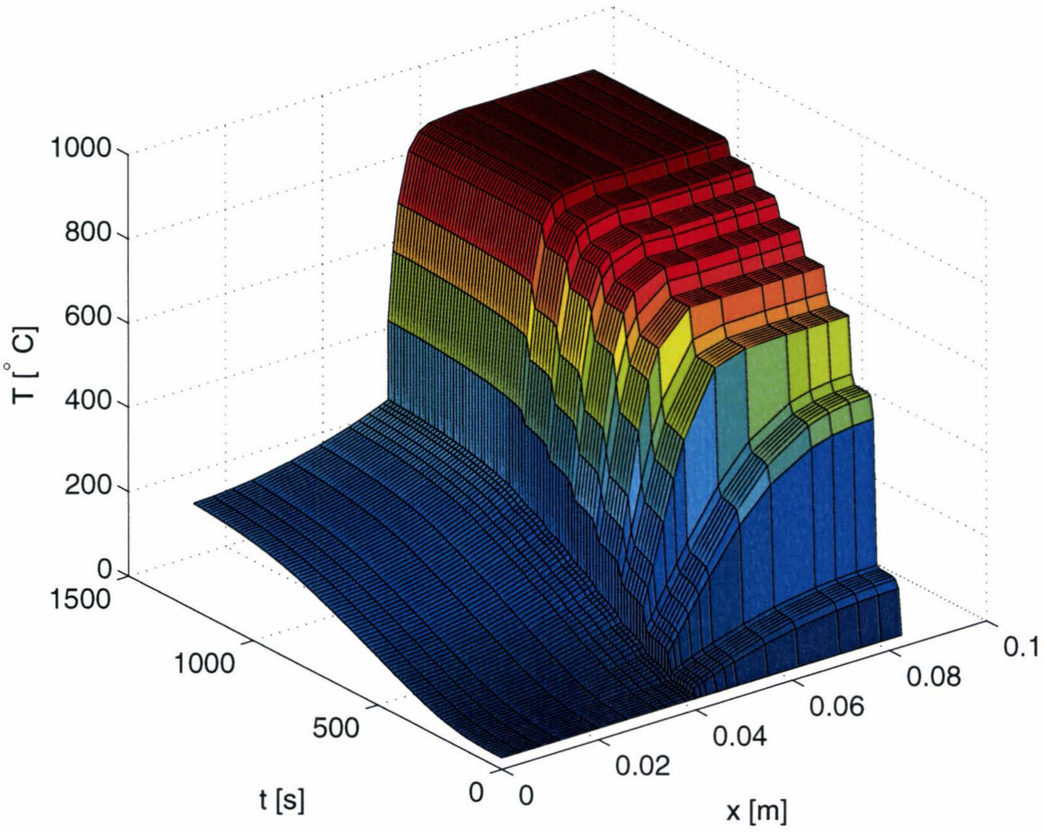

Figure 3.13: Simulated temperature profile over the heater assembly, as function of time

electrical insulation, a first layer of thermally conductive, electrically insulating ceramic adhesive (Ceramabond 865, Aremco)is applied to the heater, followed by an appropriate drying and curing cycle. Then the thermocouple junctions are pressed against this now insulating layer and a second layer of adhesive is applied. This procedure is found to provide good electrical insulation.

The steel blocks are in this configuration rotated with respect to the heater, and this is taken into account by changing the block's dimensions: assuming again symmetry, and one-dimensionality, model length is taken half the actual length and model width is taken twice the width. The surface hereby lost surface area is ignored.

Figure 3.14: Substrate equipped with five thermocouples. Dashed white line indicates clamped region of substrate

A satisfactory match between model and measurement is found, deviations are probably due to inaccuracies in the exact resistivity as function of temperature, and convection coefficient or emissivity. Emissivity depends on temperature, as stated before [Jai71], but is assumed constant. This is not further investigated, because the general behavior is mimicked very well by the model over the whole temperature range.

Zooming in on the rapid heating upon the step in current, it is clear that measured temperature lags simulated temperature. This may be due to the ceramic adhesive by which the thermocouple is attached to the substrate. This local thermal mass may be

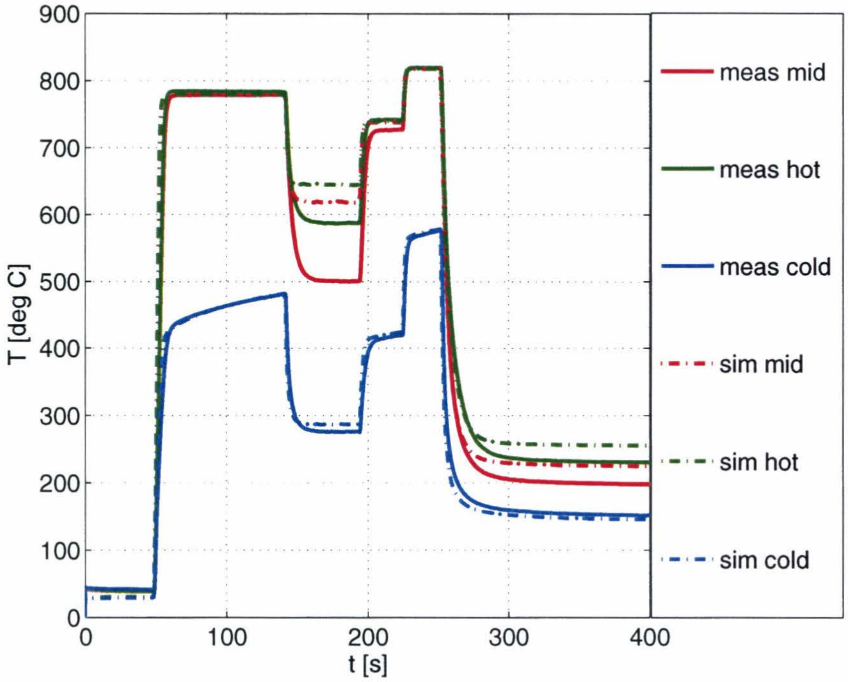

(a) Temperature

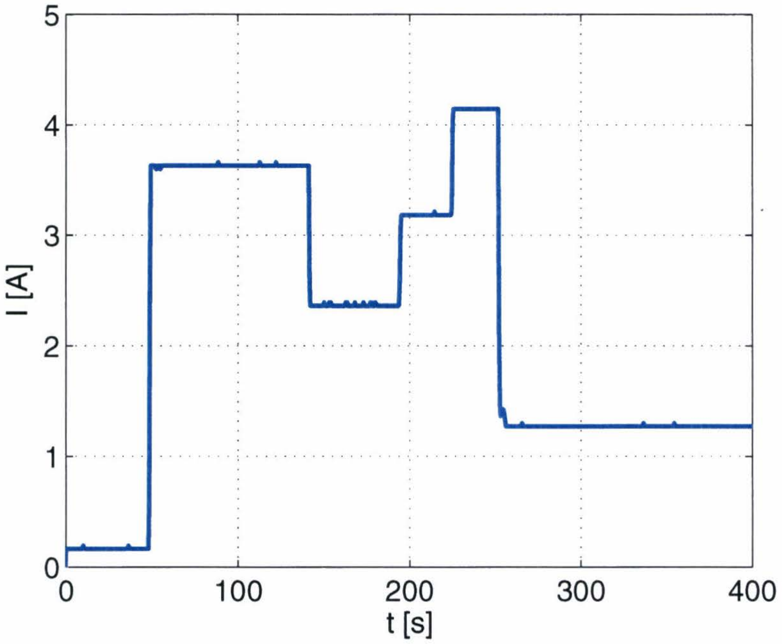

(b) Input current

Figure 3.15: Measured and simulated response to a measured input current

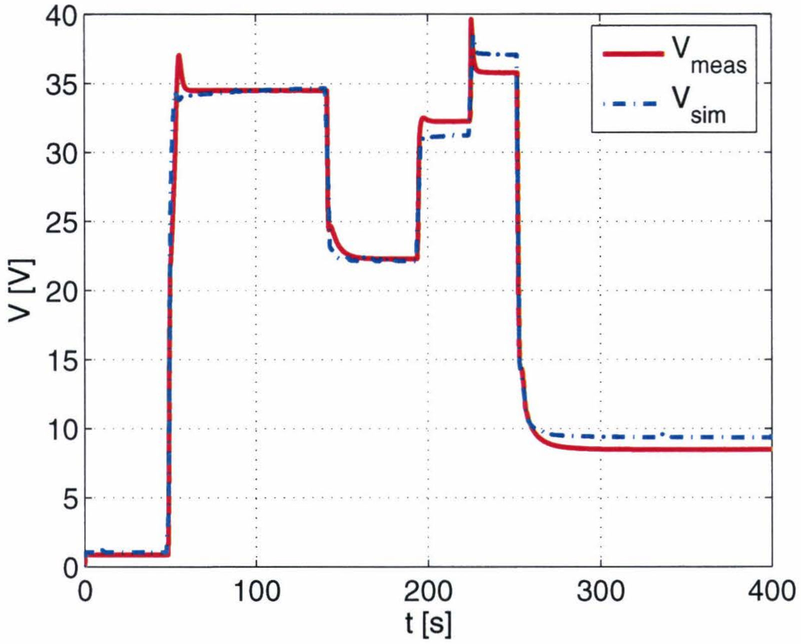

Figure 3.16: Measured and simulated voltage response to a measured input current (see Fig. 3.15(b)

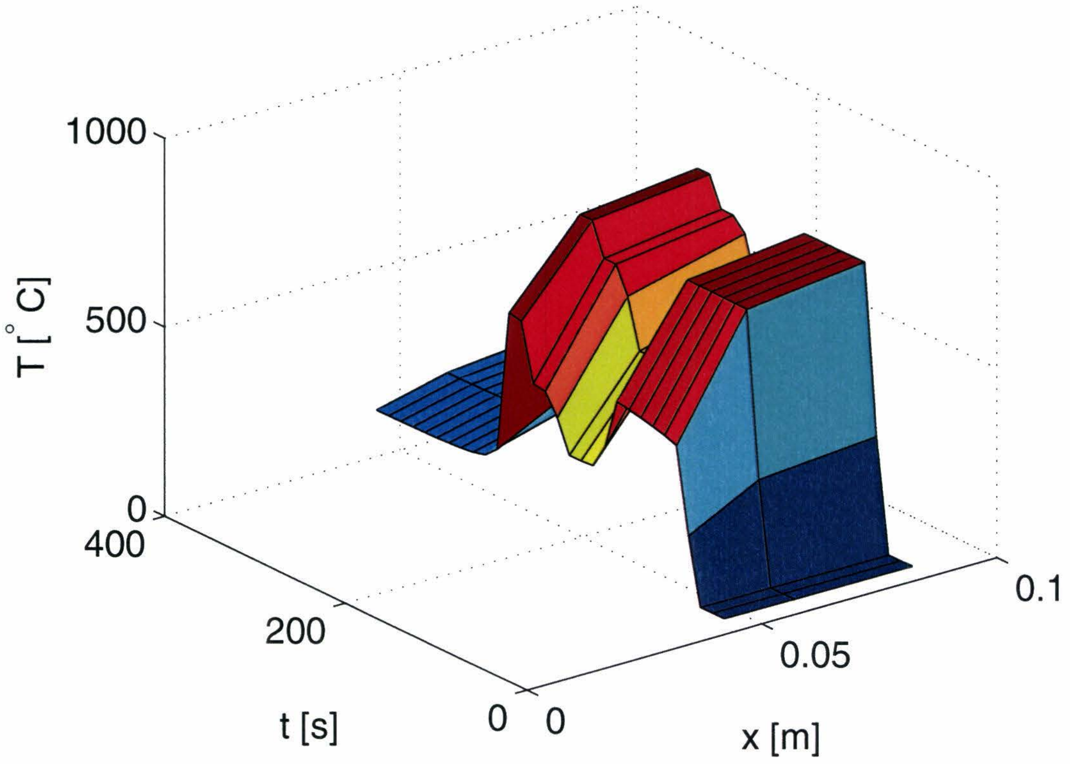

(a) Measured temperature profile

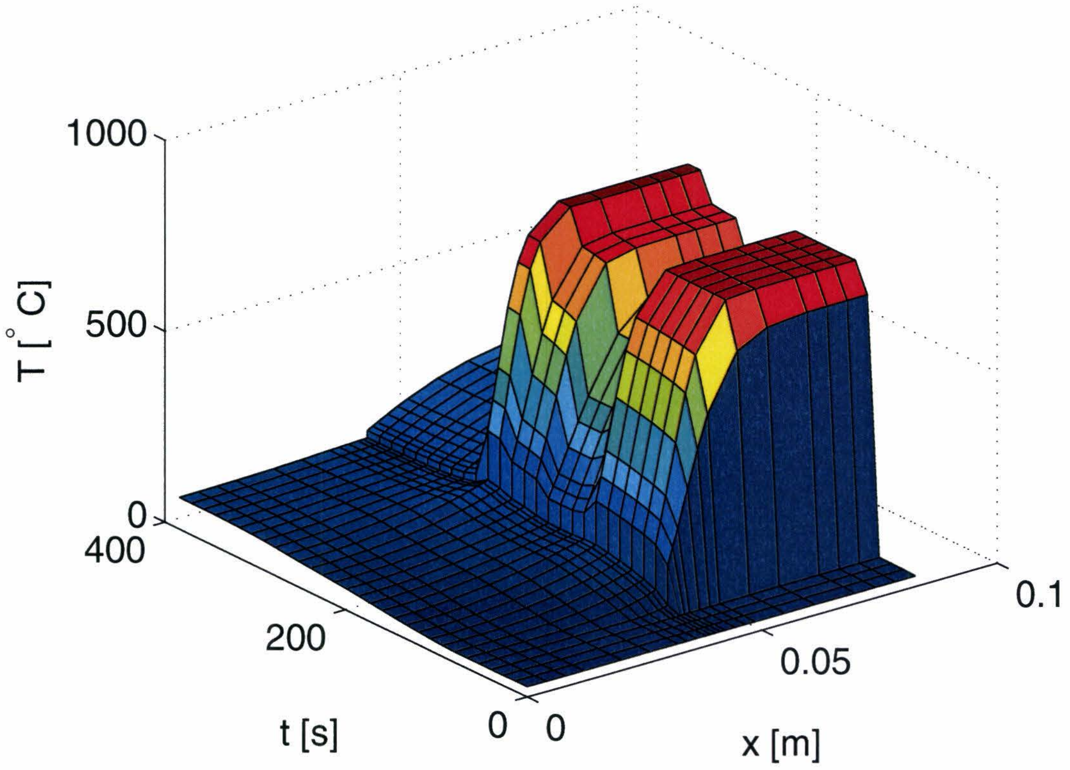

(b) Simulated temperature profile

Figure 3.17: Simulated and measured temperature profile over the heater assembly, as function of time

neglected for the behavior of the whole substrate at lower rates of temperature change, but influences the thermocouple readout during rapid heating and cooling.

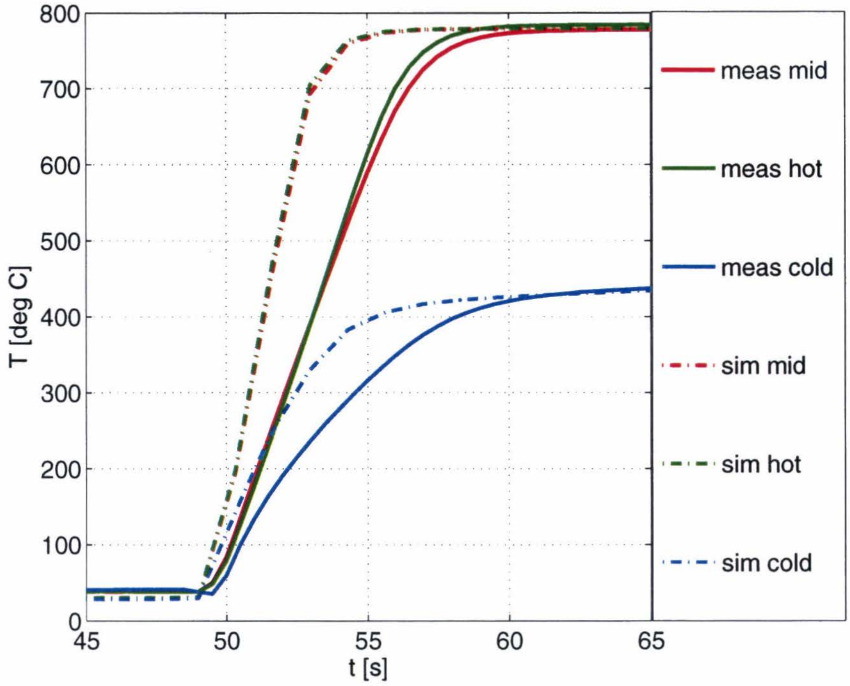

Figure 3.18: Simulated and measured temperature, as function of time. Lag of thermocouple readout

3.5.7 Applicability to the micro-channel device

It is concluded that the proposed method should work for a directly heated substrate based on scaling of the energy conservation equation and numerical simulation. The heater should also be able to heat a regular substrate with or without a "cap", or the micro-channel device when placed onto it. This situation is modeled by separating the cross section that conducts electrical current ($A_{HH,elec}$) from the cross section that is heated (A_{HH}). By specifying cross-sectional dimensions as a function of x, the extra thermal mass, as well as cooling surface and conducting cross-section, is locally added. No extra domain is necessary if the thermal contact between the two optically flat surfaces is assumed perfect. The block current analysis is repeated for the micro-channel case only, because this is the larger load between the regular substrate and the micro-channel device. The width of the heater is taken 19 mm, equal to the width of the device. Height of the micro-channel device is taken 3 mm including the heater element (0.3 mm), catalyst substrate (0.4 mm), micro-channel device (1 mm), and some thermal mass representing a ceramic plate and binder clips to clamp the assembly together. The amplitude of the block current is 8 A, as opposed to I =4 A used before.

Heating from room temperature to 800°C takes ≈23 s. Cooling down from 800°C to 300°C takes ≈17 s. The continuous input power is $P \approx 280$ W at a voltage of $V \approx 35$ V. The peak voltage $V_{max} \approx 45$ V

Plotting again the temperature profile as function of time clearly shows the effect of the local thermal mass of the micro-channel device. Again, by the natural feedback mechanism the profile is flattened, and after the initial lag temperature is almost constant over the center of the heater.

3.6 Next generation apparatus

The setup as analyzed in the previous section 3.5 has been produced and using this simple setup regular substrate experiments have been carried out, that will be described in the next chapter 4. In the current chapter, the design and fabrication of a more developed furnace is reported. This apparatus improves access to the substrate for easier setup and in-situ monitoring and it accommodates larger substrates for use with the micro-channel device.

3.6.1 Design objectives

Set-up and operation of the heater assembly inside a quartz tube is sometimes cumbersome. Installation of a thermocouple or placement of the samples, especially in the "capped" configuration, can be time-consuming. The first design goal for the new setup is then to improve access to the heater for installation before an experiment.

A consequence of not using a tube furnace, but only a quartz tube (to provide of course the necessary sealed environment), is that the substrate is open for optical observation. This feature is considered very valuable and must be continued in the new setup.

Measuring temperature with a thermocouple may hinder future experiments. It is noted that the chromel and especially alumel legs themselves catalyze hydrocarbon decomposition. As a consequence, although they perform well in an inert environment, their accuracy can not be guaranteed in the reducing environment of growth experiments. Therefore, a different means of temperature measurement is needed.

The micro-channel device needs a wider and longer heater than regular substrate experiments. Also, a means for clamping the channel device to a catalyst substrate must fit into the new apparatus.

Lastly, to accommodate future changes, the setup should be as flexible as possible in terms of gas supply, instrumentation, and mechanical access during experiments.

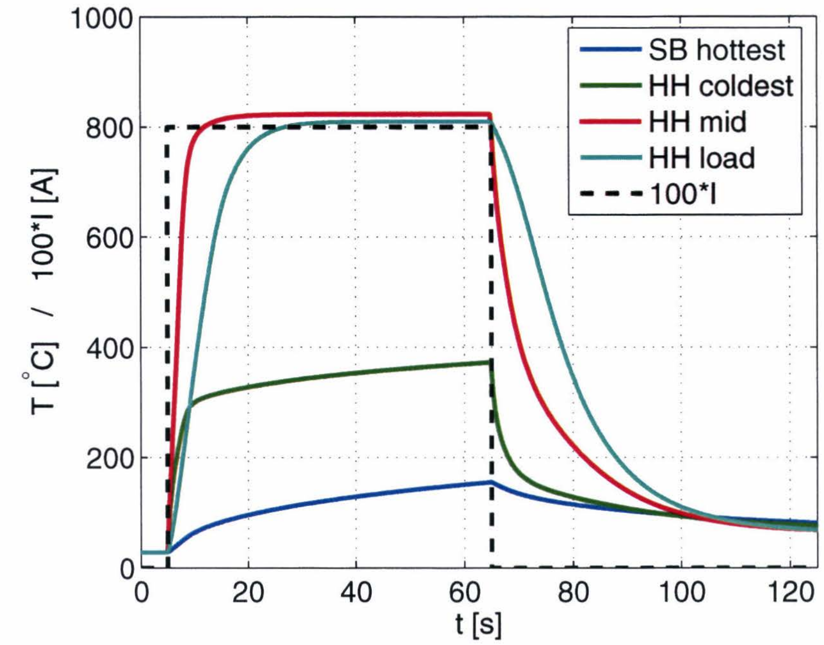

(a) Simulated temperature of selected nodes

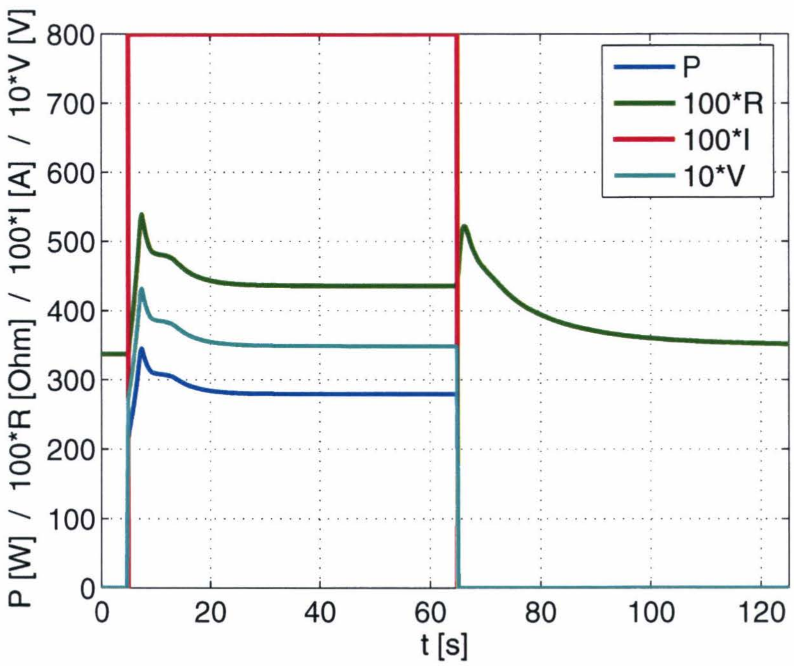

(b) Simulated resistance, power, and voltage

Figure 3.19: Response of proposed system, with micro-channel device, to 8 A block current

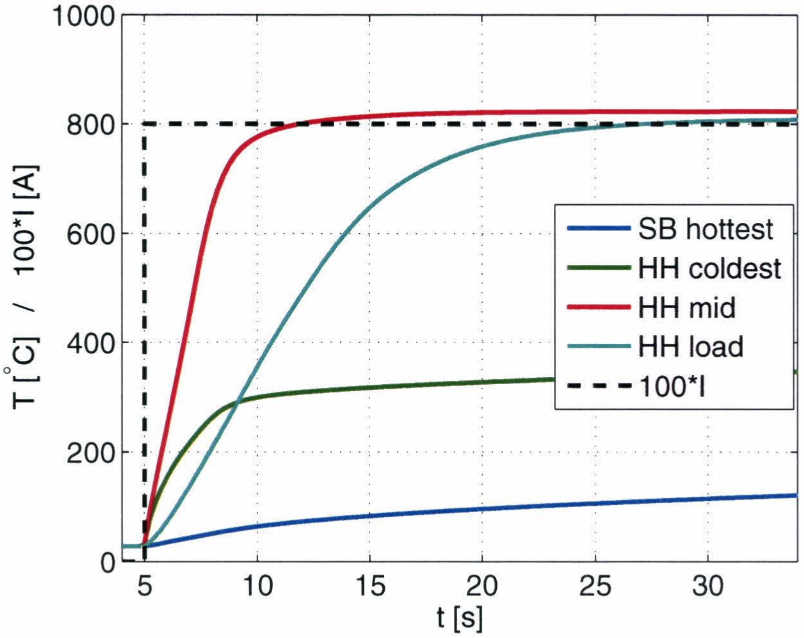

(a) Zoom of heating

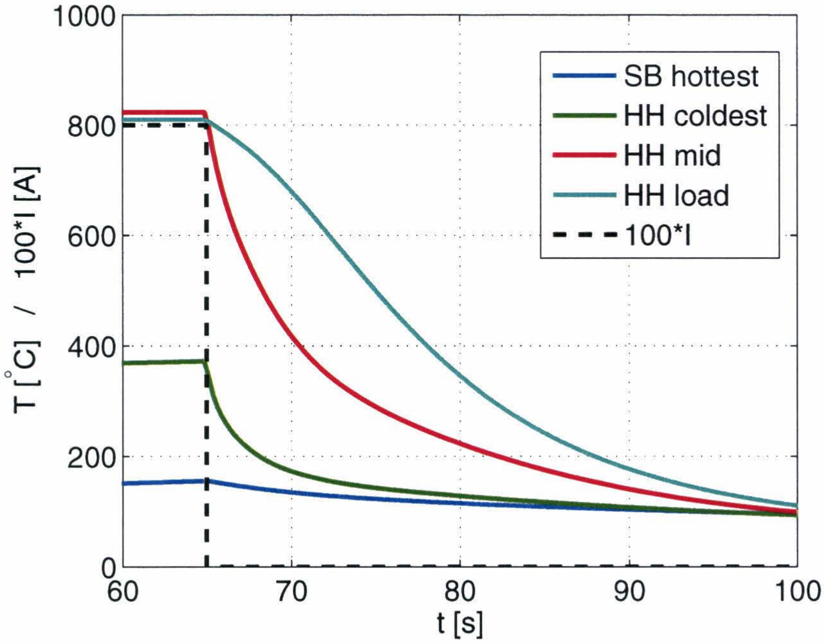

(b) Zoom of cooling

Figure 3.20: Response of proposed system, with micro-channel device, to 8 A block current

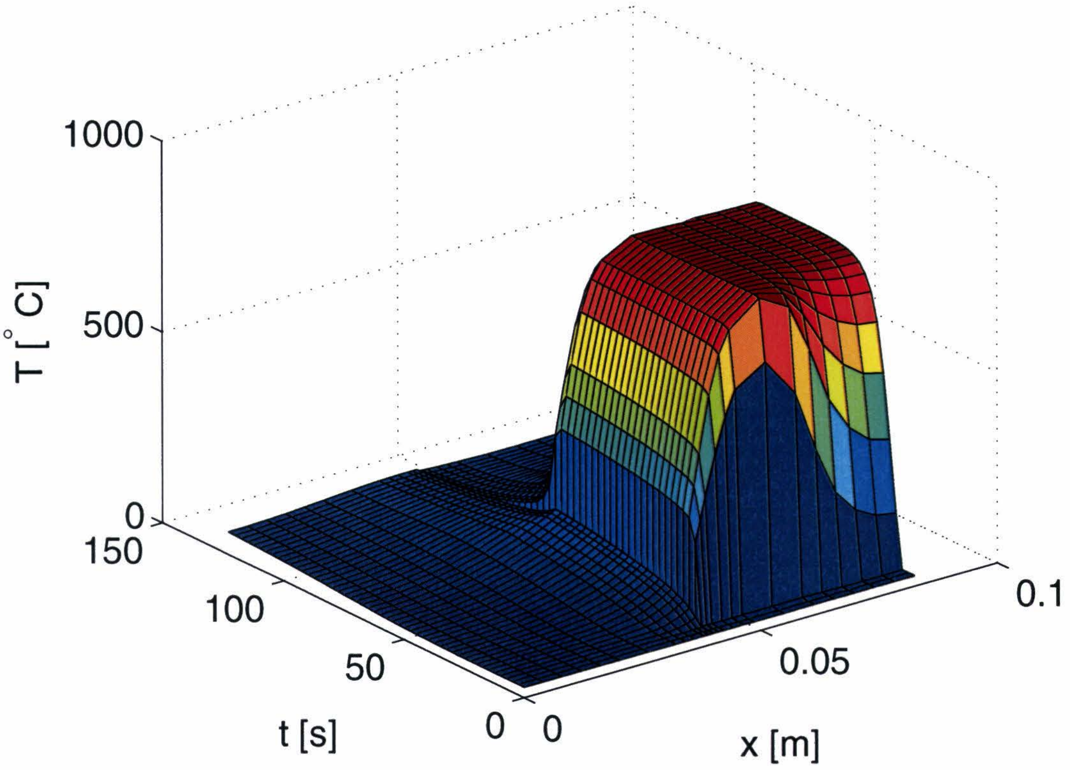

Figure 3.21: Simulated temperature profile over the heater assembly, including the micro-channel device

3.6.2 Proposed design furnace apparatus

A simple and functional solution is found in a clam-shell aluminum enclosure, with Pyrex windows for optical access, as shown in Fig. 3.22. Overall dimensions are 200×200×150 mm.

Gas and electrical feed-throughs are provided in the stationary sidewalls. The removable top is sealed to the bottom by an o-ring face seal and held by latches.

The heater element is placed perpendicular to the gas flow, to have the most predictable flow, not having the steel blocks in the gas-stream before and after the substrate, but on the sides. To save space then, the blocks are rotated with respect to the heater, forming an H-shape with the heater.

The steel blocks must be supported, while allowing for different heater sizes and thus different spacing between the blocks. Two electrically insulating ceramic rods function as supporting rails, allowing for a wide range of heater lengths.

For regular substrate experiments, gas is supplied from a quartz tube, long enough to provide a developed flow. Excess gas is removed through gas-outlets at underpressure.

When using the micro-channel device, gas may be delivered to the atmosphere through that same tube, where a quartz tube brazed to a quartz plate is clamped to the substrate provides the underpressure to draw the gases in. Alternatively, reactants may be delivered directly to the substrate through another quartz tube. In either case, a quartz plate, cut out of quartz with optical surface finish, is clamped on top of the stacked heater element–catalyst substrate–micro-channel device.

Non-contact temperature measurement of the silicon heater is provided by an IR-thermocouple that is focussed on a 3 mm spot. This kind of sensor has a wide spectral response of 0.1-5 μm. Silicon emissivity is low at wavelengths higher than 0.7 μm, so care must be taken to obtain a high enough signal-to-noise ratio. The Pyrex window used is not transparent at wavelengths higher than 2 μm, cutting off a big part of the unwanted spectrum. However, if the window heats up, it may contribute an error signal. The window is not in focus, and no significant error is expected.

An even better, but more expensive solution would be a silicon element. This type of sensor is available with a spectral response centered in a small band around 0.7 μm. At this wavelength silicon has high and constant emissivity.

Another figure, including the IR-sensor is attached as Appendix D.

3.7 Summary

- The design objective for a new furnace apparatus is rapid heating and cooling with 40°C/s

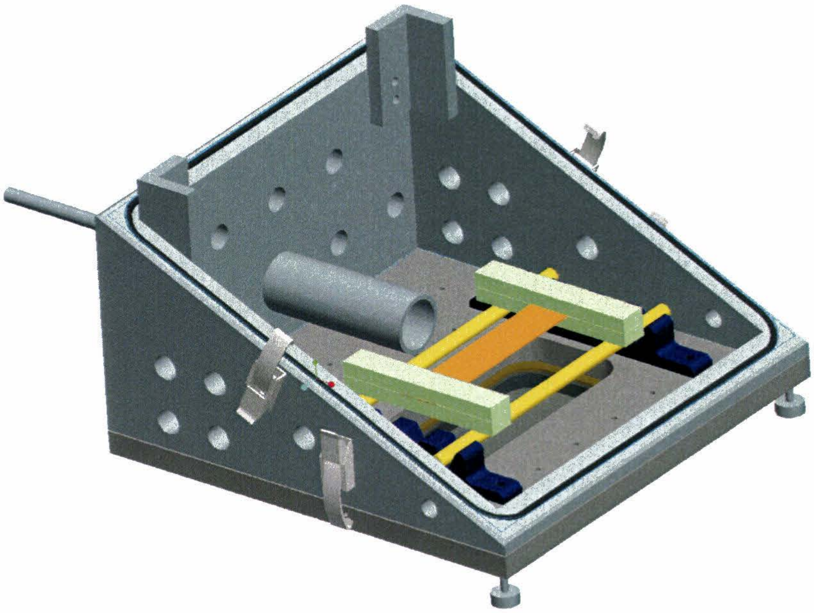

(a) Enclosure in opened position (during installation)

(b) Enclosure closed (during operation)

Figure 3.22: Clam-shell enclosure

- Resistive heating of a silicon substrate is selected as the best heating method
- A setup consisting of a silicon heater element clamped by steel blocks is proposed and analyzed. Based on simulation, specified heating rates are achieved. Verification by measurement shows a satisfactory match between model an measurement
- A next generation setup is proposed, based on a simple aluminum clam-shell design

Chapter 4

Experimental results

Experimental results from the resistive heater setup are presented. Growth as function of substrate temperature is briefly studied. An impressive increase in aligned MWNT growth rate and ultimate length is achieved by preheating the reactants, and growth is monitored by optical photography and video.

Fig. 4.1 shows the setup that is used in all experiments. A 48 mm quartz tube is sealed off by aluminum endcaps, with feed-throughs for gas and electrical connections. The tube is supported on aluminum V-shaped stands. High purity gases are supplied from cylinders close to the setup and metered by calibrated rotameters. Exhaust gas is passed through a bubbler and vented.

The sample is placed on the heater element and in the "capped" configuration a nitride-covered substrate is placed on top with a non-polished nitride surface resting on the catalyst layer. This cap alters the flow conditions favorably and doesn't seem to hinder consecutive growth as it is lifted up by the growing CNT. All experiments reported in this chapter are in the "capped" configuration, where sometimes the nitride cap is replaced by a quartz cap for in-situ observation.

4.1 Aligned MWNT

Growth of aligned MWNT is studied in a recipe using iron on alumina as the catalyst layer and ethylene as the carbon feedstock. The general recipe is:

1. atmospheric gas is displaced from the tube by flushing with 400 sccm Ar for 10 minutes
2. temperature of the heater is ramped to the setpoint in a few seconds, while 400 sccm Ar is continued
    - typically 750°C. The temperature is controlled by keeping a constant current.

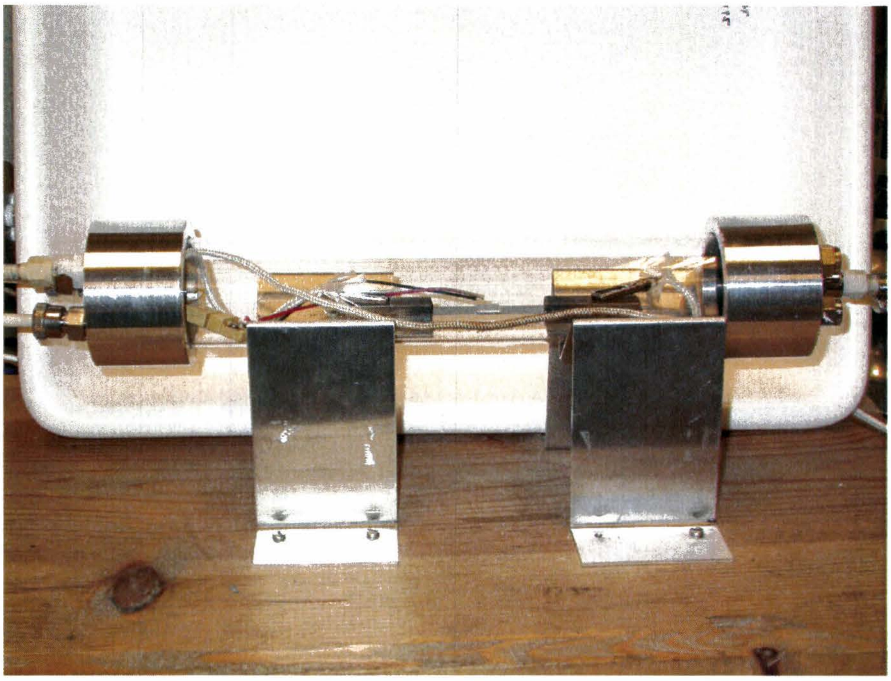

Figure 4.1: Setup used for regular substrate experiments

3. 400 sccm Ar is continued for another 2 minutes
4. reaction species are introduced for the duration of the experiment
    - H_2 is introduced 1 – 5 minutes before carbon feedstock
    - typically 15 minutes
    - typically 100/400/200 sccm $C_2H_4/H_2/Ar$
5. heater is turned off and 400 sccm Ar is introduced for 5 minutes

4.1.1 catalyst preparation

Catalyst substrates for MWNT growth are prepared by e-beam deposition of 20 nm Al_2O_3 followed by 1.2 nm Fe on 6" Si wafers. Patterned catalytic layers are made by a lift-off method: a photoresist layer is patterned by photolithography and the catalytic layer is deposited. The areas of catalyst on photoresist are removed in acetone and a patterned catalytic layer remains on the wafer [Har06]. Samples are made by scraping with a diamond-tip pen and breaking. Unless indicated otherwise $\approx 10 \times 10$ mm samples are used. The samples are prebaked in a tubefurnace under 400 sccm Ar. Temperature is ramped to 750°C in 30 minutes and held for 15 minutes.

4.1.2 Temperature

Preliminary attempts to grow CNT on the substrate heater resulted in thin tangled films. A short study of the effect of temperature resulted in the first aligned growth. Temperature was monitored before the experiment by a thermocouple cemented to the heater, but during experiments measurements were disturbed by the reactants. In fact, carbon deposition was catalyzed by the thermocouple wires themselves. Temperature was therefore measured before experiments and assumed constant during experiments by controlling the current. SEM inspection of produced films shows that best growth occurs for $T \approx 750°\text{C}$. The highest measured film thickness was 175 μm at 750 °C.

Fig. 4.2 shows the fibrous carbon deposited on the alumel leg of a thermocouple. Alumel is an alloy consisting of 95% nickel, 2% manganese, 2% aluminium and 1% silicon. It shows fibers divided by a flat cylindrical particle, typical for growth from "bulk" (dimensions much larger than nanometer-scale) steel, iron , and nickel (John Hart unpublished results, and [Zen05]. The same fibers were also found when a high purity Ni mesh was heated on top of a catalyst sample on the resistive heater. The intention of this experiment was to possibly "activate" the carbon feedstock by partial decomposition at the nickel mesh, but in stead carbon deposited in the form of thicker fibers on the nickel mesh only.

Figure 4.2: Fibrous carbon grown from alumel thermocouple wire

Fig. 4.3 shows an SEM image (tilt angle 70°) of a sample grown at 750°C in 15 minutes. H_2 pre-treatment time was 5 minutes. Film thickness is 102 μm.

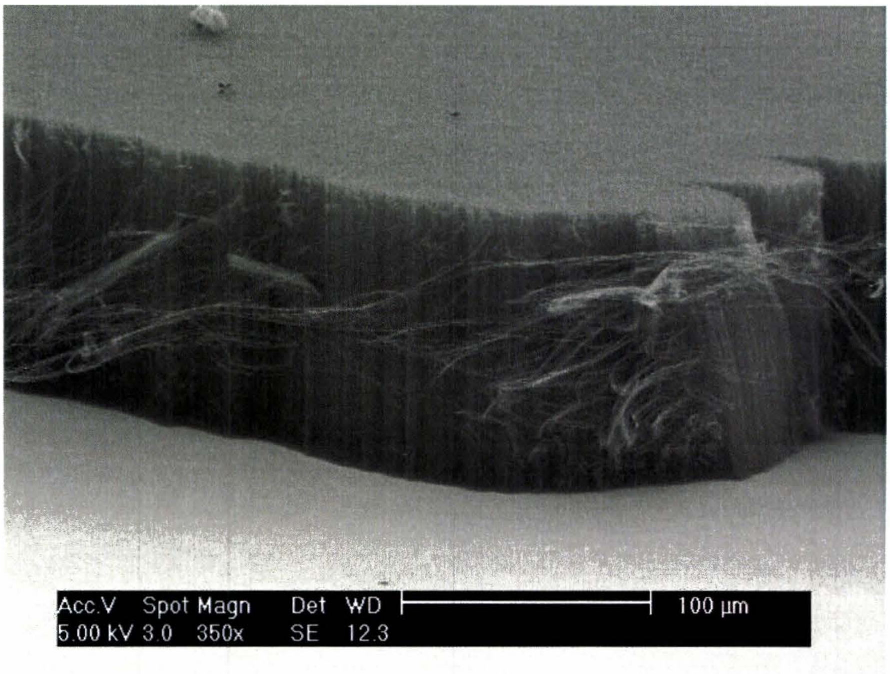

Figure 4.3: Aligned MWNT grown from $C_2H_4/H_2/Ar$ in 15 minutes at 750°C

4.1.3 Gas pre-heating

First aligned growth proved the principle, but growth rate was lower than in a regular tube furnace process. In the resistive heater setup gas is only heated upon contact with the substrate, while in a tube furnace reactants are heated for approximately 30 seconds before reaching the substrate. In an attempt to replicate growth achieved in a regular setup, reactants are passed through a tube furnace heated to 750°C before being introduced into the resistive heater setup. Although the gas cools almost to room temperature between exiting from the tube furnace and entering the resistive heater tube, substantial improvement in growth rate and ultimate length results: the gas is "activated" by heating to 750°C, and stays in this more active state after cooling. Aligned films of over 1 mm now grow in 15 minutes.

By a different means of pre-heating the reactants, another improvement is achieved. An Nichrome resistance wire is wrapped around a four-bore alumina tube (outside diameter 1/4"≈6.4 mm, bore diameter 1/16"≈1.6 mm, length 12"≈300 mm) over a length of 100 mm. Reactants are fed to the quartz tube through this alumina preheater tube. The alumina tube is heated by applying a voltage to the resistance wire ($V \approx 30$ V, $P \approx 100$ W). A temperature inside the preheater of approximately 1100°C, as measured ex-situ by a thermocouple, is found to improve growth significantly. This may be surprising, as in atmospheric CVD processes temperature is normally kept below the pyrolysis temperature of the hydrocarbon, to avoid deposition of amorphous carbon that could terminate growth and pollute the product. In fact, soot formation occurs in the preheater, and some soot is carried into the tube by the gas flow, but it does not reach the substrate and therefore does not interfere with CNT growth. Still, it is interesting to note that by heating the precursor higher than its pyrolysis temperature, the gas that does not decompose is more active when it reaches the catalyst substrate.

Fig. 4.4 shows an SEM image of the sidewall of a sample processed in the alumina preheater configuration. Aligned growth is observed with a uniform thickness of 1.7 mm, except for an extra tall pillar, shown in topview in Fig. 4.5. In various other experiments, growth is found to be less than perfectly uniform. Typically, growth is either aligned and tall, or tangled and limited to tens of microns thickness, but both regimes may occur on the same sample. Which one occurs is believed to be determined by the presence or absence of favorable conditions at growth initiation. If not enough active species are present from the beginning, a tangled forms and aligned growth is inhibited at that location. If aligned growth does occur, it happens either as a continuous film, or in the form of cylindrical pillars. The round cross-section of the pillars again points to an "inverse loading effect", referring to the fact that CNT growth is favorably influenced by other nearby growing CNT [Har06]. Here, since neighboring CNT are actually touching, a mechanical effect may also contribute to the growth enhancement. In general, aligned growth is believed to be caused by a "crowding effect", meaning that rapidly growing CNT have no other way to go than upward in the same direction. There certainly is a strong mechanical coupling between touching nanotubes, due to Van der Waals forces. Therefore, the shape of the protrusion shown in Fig. 4.5 could indicate that growth is enhanced by "pulling forces" during growth. This was also suggested by John Hart based on other observations, including that growth decreases under a mechanical load (John Hart, unpublished results).

4.1.4 In-situ film thickness observation

One of the mayor advantages of the substrate heater setup is that the substrate is available for optical observation. Combined with the high growth rates, and resulting millimeter-scale films achieved in the process with alumina preheater, this enables in-situ monitoring of film development and thickness by optical photography. Two configurations for optical monitoring have been used: "topview" – using a quartz cap the development of the film is observed; and "sideview" - film thickness is monitored, either a transparent or an opaque cap can be used.

Two examples of in-situ observation are shown. A series of topview images, showing initiation and development of a film witnessed through a quartz cap, and a series of sideview images demonstrating rapid growth of the film. The pictures are taken through the curved sidewall of the quartz tube, so the results must be interpreted carefully. At present, it is not clear wether or not the film thickness increases linearly with time, as is suggested by the sideview images, as the images may be distorted by diffraction at the quartz-air interface.

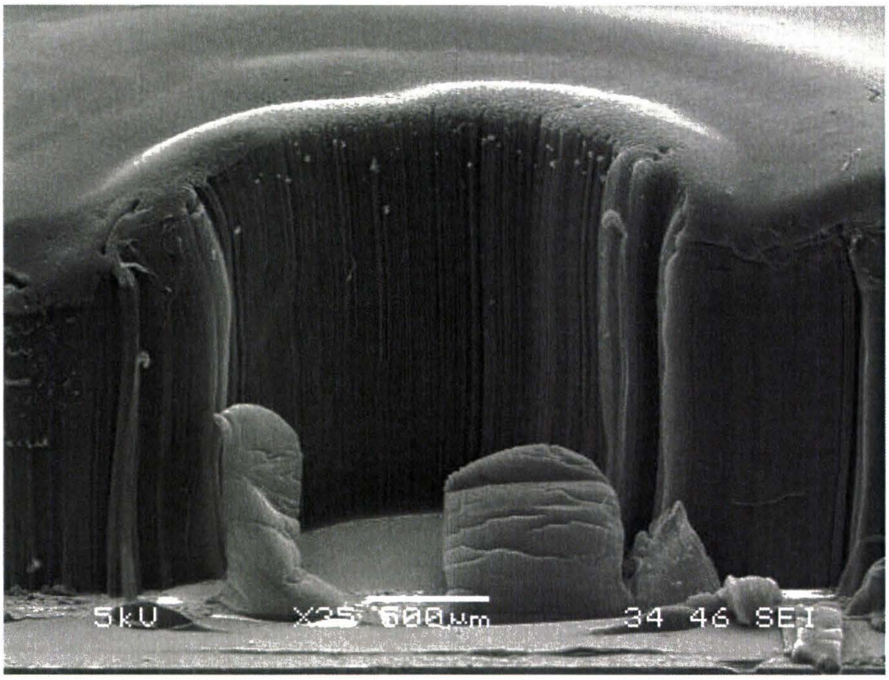

Figure 4.4: Aligned MWNT grown from $C_2H_4/H_2/Ar$ in 15 minutes at 750°C. Preheater at 1100°C

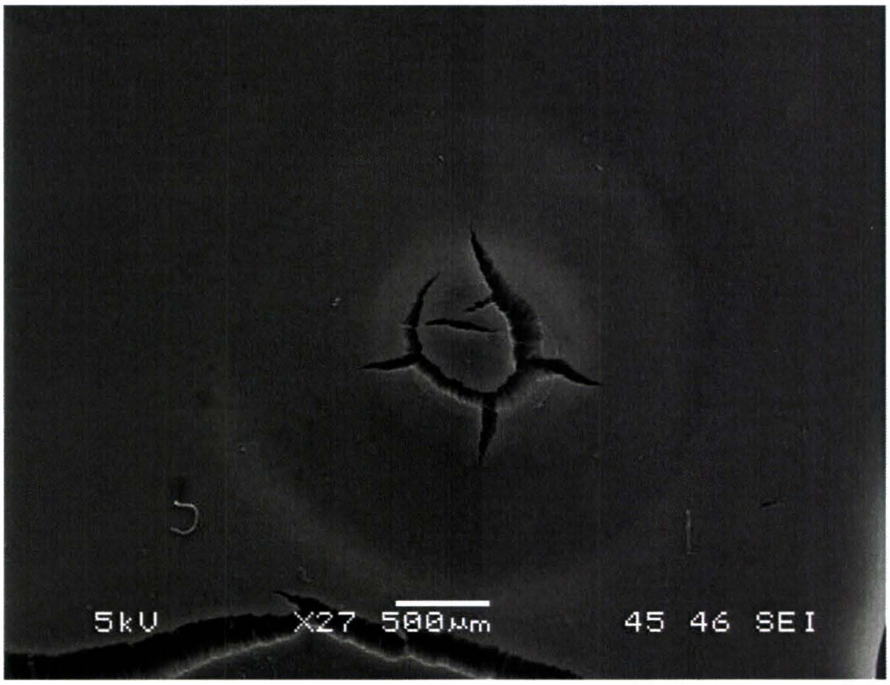

Figure 4.5: Aligned MWNT grown from $C_2H_4/H_2/Ar$ in 15 minutes at 750°C. Preheater at 1100°C. Locally taller growth has a circular shape

Fig. 4.6 shows a selection out of a series of images taken with a digital camera equipped with professional zoom lenses through a quartz cap resting on the growing film. Inspired by results reported in [Rod93] where increased decomposition of ethylene over an iron catalyst was observed upon adding CO to the gas mixture, Ar was replaced by CO during the reaction time. The result was an increase in growth rate and less uniform growth. Crack formation is observed, likely due to stresses caused by non-uniformities in growth rate.

Also observed is a color change in the region where catalyst is deposited within the first 15 seconds. It can be concluded that growth starts shortly after introduction of the reaction species.

Fig. 4.7 shows a selection out of a series of images taken from the side of a growing CNT film. A series of pictures taken with constant interval of 5 minutes shows that growth appears to be linear. This is interesting in light of findings reported on SWNT, where many experiments were conducted with increasing growth times to create plots of thickness as function of time [Fut05]. It was clearly shown there that SWNT length exponentially approaches a final value. If these measurements are accurate, it indicates that either growth was not yet close to self-termination when the reaction was stopped after 20 minutes, and a longer experiment could result in much taller growth, or a different mechanism of growth termination occurs in this setup, compared to the (otherwise very similar) setup reported in [Fut05], due to the different heating configuration. But, as mentioned, care must be taken in interpreting these results, as the pictures are taken through the curved wall of the quartz tube, and may be distorted.

4.1.5 Rapid heating

Rapid heating has so far been useful because it shortened experiment time. Separating substrate temperature and gas (preheating) temperature has improved growth rate and ultimate length. Rapid heating however has not been extensively studied. Preliminary tests were conducted as follows.

In stead of heating the substrate first, and next introducing reactants, $C_2H_4/H_2/CO$ or $C_2H_4/H_2/Ar$ is introduced first, followed by rapid heating of the substrate. Aligned growth occurs in pillars around the edge of the substrate, but no continuous film forms.

H_2 pretreatment of the catalyst is critical to obtain dense aligned CNT growth. Therefore, the recipe is altered.

1. atmospheric gas is displaced from the tube by flushing with 400 sccm Ar for 10 minutes
2. Ar/H_2 is introduced for 7 minutes
3. 2 minutes after introducing Ar/H_2, temperature of the heater is ramped to the setpoint in a few seconds, and held for 5 minutes

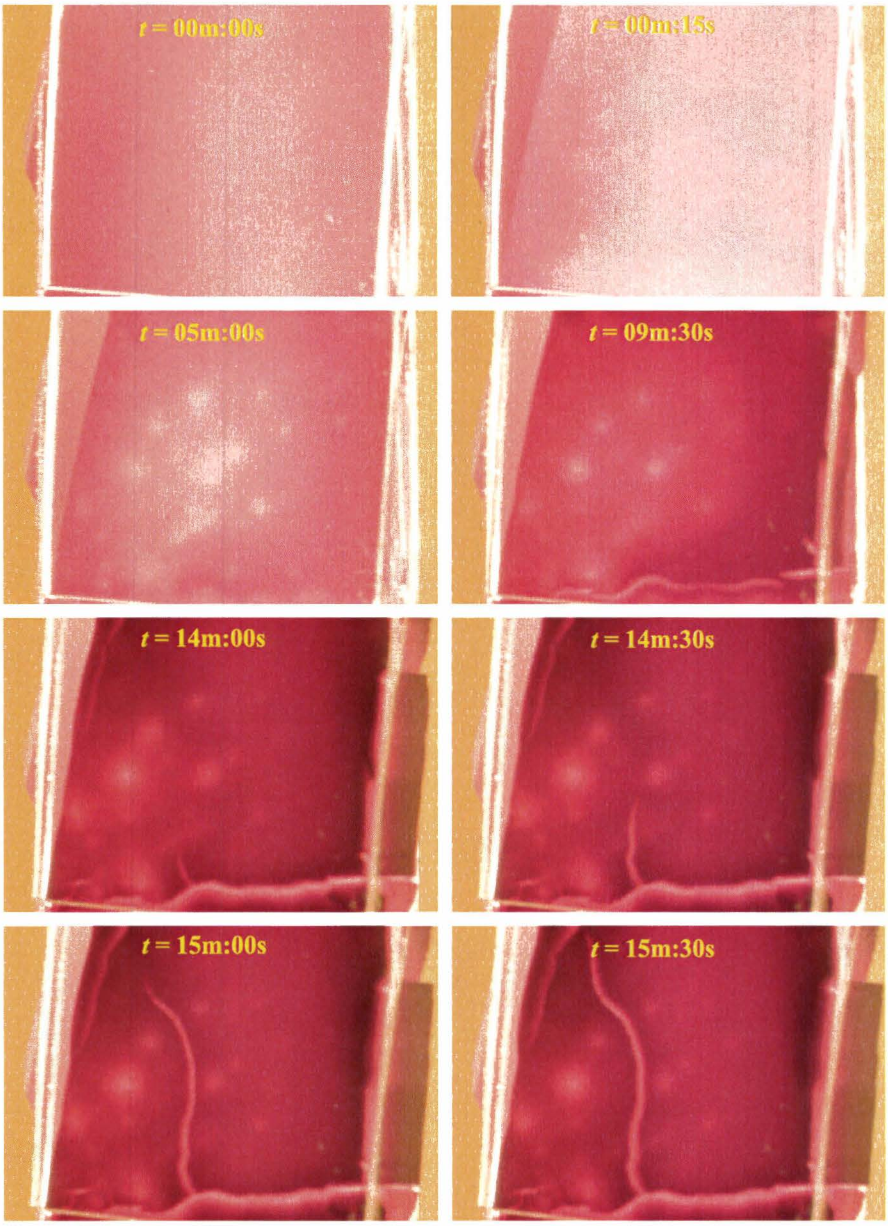

Figure 4.6: Topview optical images of growing aligned MWNT film. Growth from $C_2H_4/H_2/CO$ in 20 minutes at 750°C

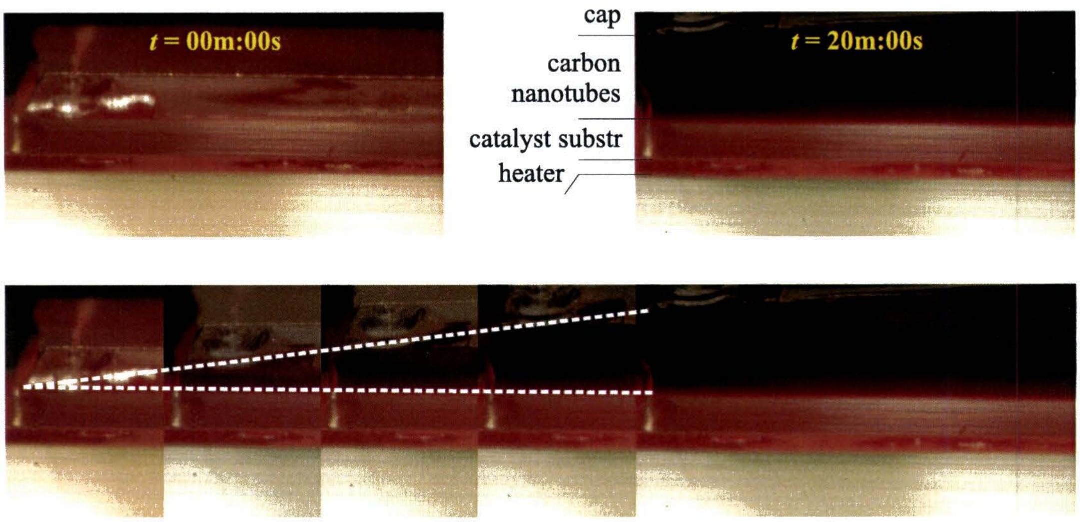

Figure 4.7: Sideview optical image of growing aligned MWNT film. Growth from $C_2H_4/H_2/CO$ in 20 minutes at 750°C

4. $C_2H_4/H_2/Ar$ is introduced for 2 minutes, plus the reaction time
5. After 2 minutes, the heater is ramped to the setpoint temperature, and held for the reaction time (15 minutes)
6. The heater is turned of, and 400 sccm Ar is introduced

Using this recipe, a uniform layer of 2 mm is grown. However, no significant difference between rapid heating and normal heating is noted. It is shown that H_2 pretreatment is as critical in this system as in a regular tube furnace. However, more experiments should be carried out before the effect of rapid heating can be properly judged.

4.2 Summary

- Experiments conducted with the resistively heated setup initially show aligned growth of MWNT, but results obtained in a regular furnace are not matched
- By preheating the reactants an improvement in growth rate and ultimate length is achieved over the existing situation
- Growth using CO in stead of Ar as the carrier gas increases growth rate as well as non-uniformity

- In-situ monitoring of CNT films shows crack formation due to non-uniformities in growth rate
- Rapid heating has not shown to improve growth so far, but the separation of substrate and gas temperature has

Chapter 5

Laser heated catalyst design

The second project that is (briefly) reported, is a new laser heated thermal CVD setup, to be used at Eindhoven Technical University, after an idea by Dr. Yves Bellouard. The basis of this setup is the configuration where a catalytic layer deposited onto a silicon substrate is laser-heated from the backside. By an appropriate choice of laser wavelength and substrate material, most of the energy is absorbed in the catalytic layer, resulting in precisely located heating.

The environment must be controllable between low-vacuum ($\approx 10^{-3} mbar$) and atmospheric pressure.

The immediate application is in-situ studies of carbon nanotube growth. When the laser power is dosed so that no light is transmitted through the top surface of the sample, the top surface is available for optical observations such as Raman spectroscopy, reflectivity monitoring or ellipsometry. The controlled environment allows for parametric studies of e.g. temperature, pressure and gas flow on growth initiation, CNT extension, and growth termination.

By directing the laser beam with an x-y mirror, as is routinely done in engraving or welding applications, arbitrarily shaped patterns of CNT could be grown on continuous (not previously patterned) catalytic layers. One could fantasize that in this configuration local growth on MEMS-devices could provide localized dampening, e.g. on tethers or leaf-spring elements. Arrays of emitters could be grown only at the ends or at other specified locations of otherwise continuous catalytic metal traces. If rapid heating causes isolated SWNT to grow [Chi04], this may be employed to grow high-current interconnects, or alternatively traces of CNT could be “written” for this purpose.

The setup may also be used for the annealing of thin films, shape memory alloys, or for sample preparation for laser-assisted etching.

The setup is designed around this idea, with the purpose of providing a solid experimental platform for future studies. At present, the setup is finished, but has not yet been tested. Therefore, only the design can be presented, and no experimental results.

The optical path will be described and the vacuum chamber is briefly presented, focussing on vacuum generation and flow and pressure control.

5.1 Laser beam optical path

The beam is provided by a 10W CO_2 laser (48-series, Synrad). From the specifications, the laser beam is Gaussian with $M^2 < 1.2$. The beam diameter is 3.5 mm at the laser and the long-range divergence is 4 mrad (full angle). Wavelength is specified $\lambda = 10.60 \pm 0.03$ μm.

The goal is to focus the beam on a small spot size. If a larger spot size is needed, this can be achieved by moving away from the focus point, or "waist". A shorter focal distance or wider beam result in a smaller spot size. Working distance is limited by the geometry of the setup and it is expected that a distance of 100 mm is needed. The achievable spot size is determined using this constraint.

Geometric optics do not apply to Gaussian beams. As a striking example a Gaussian beam that has a waist at the front focal point of a lens, has a waist at the back focal plane, whereas by geometric optics a point source placed in the front focal plane should result in a collimated beam extending to infinity [Sel83]. The geometry of an ideal spherical Gaussian beam is depicted in Fig. 5.1

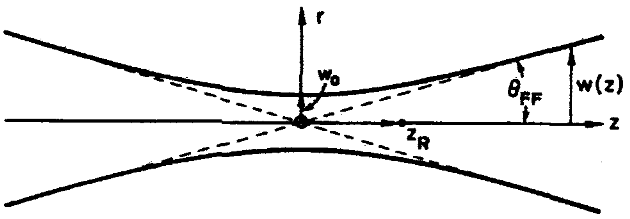

Figure 5.1: Geometry of an ideal spherical Gaussian beam ([Sel83])

The beam radius $w(z)$ [m] is defined as the radius where intensity is $1/e^2 \approx 0.135$ times the on-axis value and equals

$$w(z) = w_0 \left(1 + \left(\frac{z}{z_R}\right)^2\right)^{1/2}$$

where w_0 is the beam radius at the waist ($z = 0$), and Rayleigh range z_R equals

$$z_R = \frac{\pi w_0^2}{\lambda}$$

where λ wavelength [m].

The far-field radius w_{FF} and divergence θ_{FF} are given by

$$\begin{aligned} w_{FF} &= \frac{\lambda z}{\pi w_0} \\ \theta_{FF} &= \frac{w_{FF}}{z} = \frac{\lambda}{\pi w_0} \end{aligned}$$

Thus, far field divergence, beam radius at the waist, and wavelength are coupled. The far field angle, calculated from the specified values for beam radius and wavelength equals $\theta_{FF,Synrad} = 10.6 \times 10^{-6}/(1.75 \times 10^{-3}\pi) = 1.93 \times 10^{-3}$ Rad half angle. This matches the specified full angle far field divergence of 4 mRad.

Gaussian optics theory is used to predict the waist diameter and depth of field, arbitrarily defined as the distance where the radius is within 10% of the minimum (waist) radius.

A simple method to track a laser beam through a lens or multiple lenses is presented in [Sel83]. This method calculates for a given lens all properties of the output beam (image distance s', magnification m, and Rayleigh range z'_R) from the object distance and the input beam Rayleigh range:

$$s'/f = 1 + \frac{s/f - 1}{(s/f-1)^2 + (z_R/f)^2} \tag{5.1}$$

$$m = \frac{w'_0}{w_0} = \frac{1}{\left((1-s/f)^2 + (z_R/f)^2\right)^{1/2}} \tag{5.2}$$

$$z'_R = m^2 z_R \tag{5.3}$$

This method does not take into account spherical aberrations, or non-sphericity of the beam. A method to estimate spherical aberrations and diffraction limited waist diameter is provided on the website of II-VI infrared, a laser optics company [inf]. That method assumes that the waist is at the back focal plane.

$$D_{lens} = 2w_0\left(1 + \left(\frac{s}{z_R}\right)^2\right)^{1/2} \tag{5.4}$$

$$s' = f \tag{5.5}$$

$$w'_{0,diff} = \frac{1}{2}\frac{4M^2\lambda f}{\pi D_{lens}} \tag{5.6}$$

$$w'_{0,spher} = \frac{1}{2}\frac{kD_{lens}^3}{f^2} \tag{5.7}$$

where k is a factor that depends on the lens shape. $k = 0.0286$ for a plano-convex ZnSe lens.

Assuming the distance from the laser to the lens $s = 1$ m, from Eq. 5.3, it follows that the normalized waist distance is $z'/f = 1.05$. Thus, the waist is close to the back focal plane, and Eqs. 5.5 – 5.7 apply. Contributions of diffraction and aberration to the radius are $w'_{0,diff} \approx 140$ μm and $w'_{0,spher} \approx 0.28$ μm. Spherical aberrations are ignored. The waist diameter predicted by Eq. 5.3 $w'_0 \approx 137$ μm. This approximation is used, as it provides a better estimate of the waist distance. The depth of field is calculated by solving Eq. 5.1 for $w(z) = 1.1w'_0$. Fig. 5.2 shows the calculated beam shape, where the depth of field is highlighted.

The spot radius is smaller than 140 μm at a distance of 105 mm behind the lens. The depth of field is 5 mm, giving some room for error in the positioning of the sample relative to the lens.

5.2 Vacuum chamber

A pre-vacuum pump (Trivac D4B, Leybold) provides the low pressure, and the exhaust-flow is regulated by a manually operated precision leak valve. Pressure in the outlet duct (on the chamber side of the leak valve) is measured by two sensors spanning the whole range of pressures that can be generated in the chamber: From below 10^{-3} mbar to over atmospheric pressure. The gasflow to the chamber is regulated by precision mass flow controllers (Bronkhorst), so that by balancing the set mass flow and the precision valve leak rate, pressure and flow are both controllable. A schematic representation of the system is depicted in Fig. 5.3. A – F indicate membrane valves, mass flow controllers, vacuum chamber, pressure sensors, leak valve, and vacuum pump. 1 – 5 are the different gases delivered from the cylinders, 6 is the exhaust duct, connected to the ventilation system.

5.3 Summary

- A laser heated catalyst setup is proposed and built
- Gas flow and pressure are separately controlled

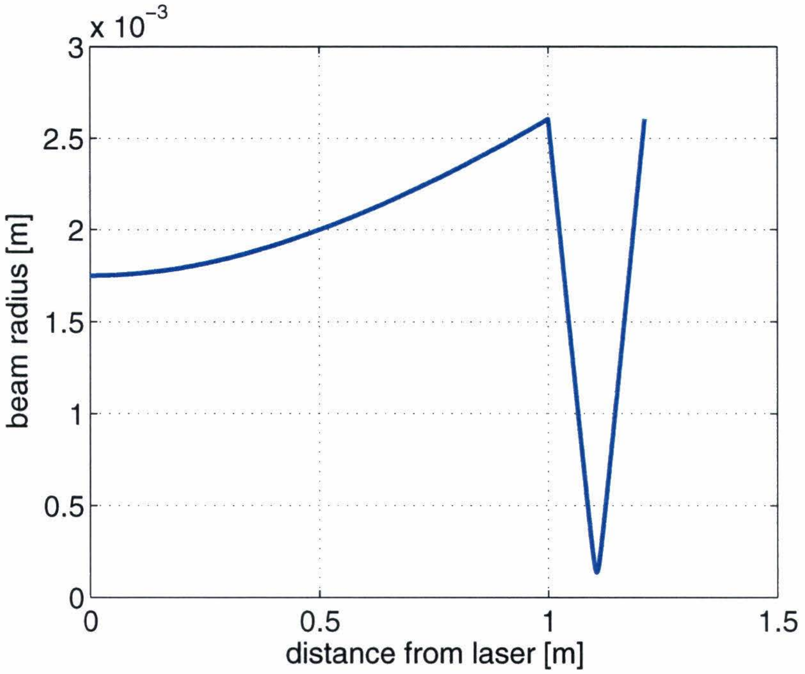

(a) Whole beam

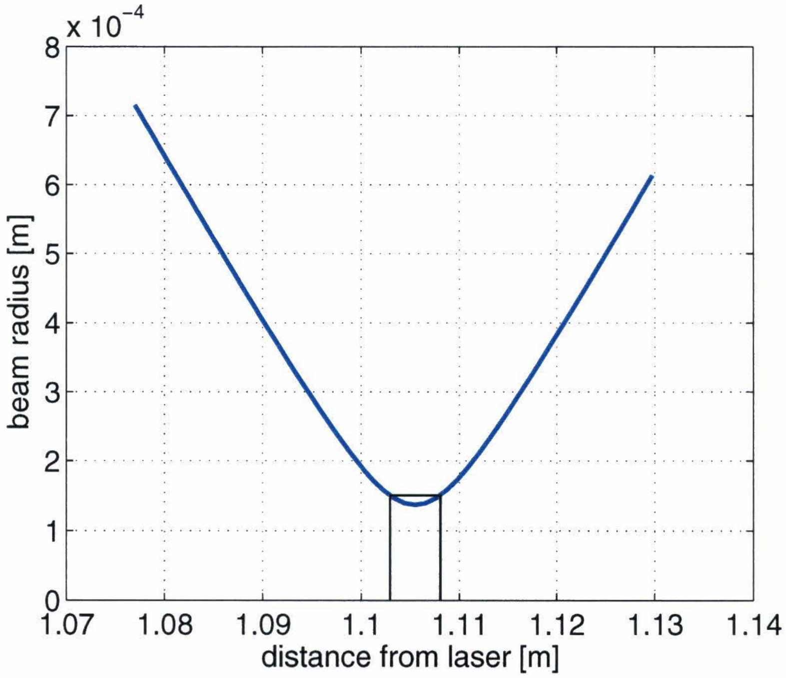

(b) Output beam around waist, black line indicates depth of field

Figure 5.2: Beam geometry for $s = 1$ m, $f = 100$ mm, with the Synrad laser, based on the Self-method

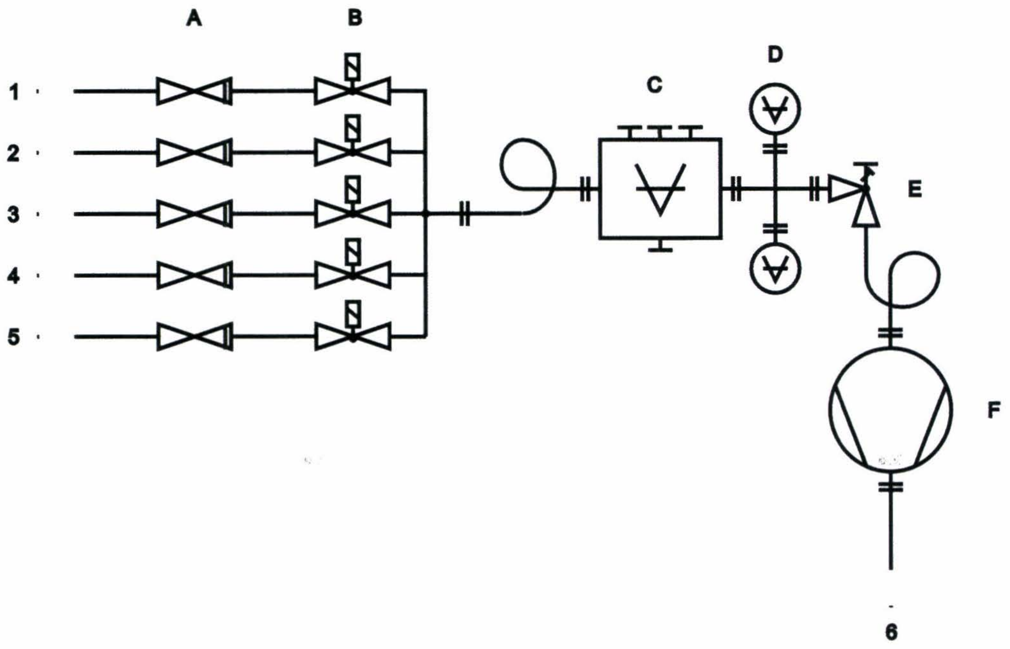

Figure 5.3: Schematic representation of laser setup: gas system

Chapter 6

Conclusions and recommendations

6.1 Conclusions

Due to vast and increasing interest in carbon nanotubes the field has advanced rapidly since the first observation in 1991. Still, many questions remain unanswered, including how to better control growth. For better control over properties and conditions, a better understanding of the growth process is critical. In-situ monitoring can contribute to the understanding of growth kinetics and formation mechanisms.

A new setup has been proposed, modeled, built, and tested and experiments have proven its value for studies of CNT growth: by separating substrate and gas temperature, an increase in growth rate and ultimate length is achieved. Also, because a tube furnace is not blocking the view at the substrate, in-situ monitoring by simple means such as photography is possible.

Preliminary results show that CNT film thickness increases linearly over 20 minutes. This may imply that much taller films can be grown using the same process but longer growth times. Alternatively, the mechanism of growth termination in this process may be different from that of reported SWNT studies.

A laser heated catalyst setup is proposed, designed and built. Gas flow and pressure are separately controllable at pressures between low-vacuum and atmospheric pressure.

6.2 Recommendations

The substrate heater as proposed may be a simple apparatus, but with proper instrumentation and careful operation it may be a very useful platform for studies of CNT growth.

The first experiment that should be done is monitoring of growth in the next generation setup. In this apparatus, that has viewports perpendicular to the substrate, unambiguous time-length curves can be generates. Experiments should be carried out until self-termination, to enable comparison with reported literature, and to shed light on the growth mechanism.

Secondly, the preheating of the gases is not well understood at present. Heating the precursor above its pyrolysis temperature causes some soot formation but also increases activity for CNT growth. The effect of this preheating step could be studied by residual gas analysis or in-situ mass spectrometry. Possibly the gas that results from the heating can be obtained otherwise, and the preheating step can be avoided. Or at least, insight in the compounds that are active in CNT growth will be gained.

Extension of the setup to the micro-channel device is currently under way. This should provide a solid platform for combinatorial studies, in combination with rapid thermal control.

Many other experiments are possible, including electrically biasing the substrate, in-situ measuring capacitance of a heated catalyst substrate with growing CNT, thermal cycling, etc.

As to catalyst preparation, it can be expected that SWNT form if accurately deposited, very thin layers of catalyst are used. The high activity of the precursor gases, in combination with such thin catalyst layers, should provide an interesting platform for studies of SWNT growth.

Further testing and installation of the laser setup is necessary, and first growth experiments should be carried out at relatively high partial pressures of hydrocarbons, possibly in combination with preheating as it can be expected, that such local growth is likely to form tangled films, if not enough active carbon feedstock is present.

Bibliography

[Bak72] R. T. K. Baker, M. A. Barber, P. S. Harris, F. S. Feates, and R. J. Waite. Nucleation and growth of carbon deposits from the nickel catalyzed decomposition of acetylene. *Journal of Catalysis*, 26(1):51–62, 1972.

[Bak75] R. T. K. Baker, G. R. Gadsby, R. B. Thomas, and R. J. Waite. The production and properties of filamentous carbon. *Carbon*, 13(3):211–214, 1975.

[Bay99] R. L. J. Bayt. Analysis, fabrication and testing of a MEMS-based micropropulsion system. *Ph.D. Thesis*, 1999.

[Ber04] C. Berger, Z. Song, T. Li, X. Li, A. Y. Ogbazghi, R. Feng, Z. Dai, A. N. Marchenkov, E. H. Conrad, P. N. First, and W. A. deHeer. Ultrathin epitaxial graphite: 2d electron gas properties and a route toward graphene-based nanoelectronics. *J. Phys. Chem. B*, 108(52):19912–19916, 2004.

[Bet93] D. S. Bethune, C. H. Kiang, M. S. Devries, G. Gorman, R. Savoy, J. Vazquez, and R. Beyers. Cobalt-catalyzed growth of carbon nanotubes with single-atomic-layerwalls. *Nature*, 363(6430):605–607, 1993.

[Chi04] S. Chiashi, Y. Murakami, Y. Miyauchi, and S. Maruyama. Cold wall cvd generation of single-walled carbon nanotubes and in situ raman scattering measurements of the growth stage. *Chemical Physics Letters*, 386(1-3):89–94, 2004.

[CIN05] CINDAS. Thermophysical properties of matter database (https://cindasdata.com/). 2003-2005.

[Dre01] M. S. Dresselhaus, G. Dresselhaus, and Phaedon Avouris. *Carbon nanotubes : synthesis, structure, properties, and applications.* Topics in applied physics, v. 80. Springer, Berlin ; New York, 2001.

[Ebb92] T. W. Ebbesen and P. M. Ajayan. Large-scale synthesis of carbon nanotubes. *Nature*, 358(6383):220–222, 1992.

[Fut05] Don N. Futaba, Kenji Hata, Takeo Yamada, Kohei Mizuno, Motoo Yumura, and Sumio Iijima. Kinetics of water-assisted single-walled carbon nanotube synthesis revealed by a time-evolution analysis. *Physical Review Letters*, 95(5):056104–4, 2005.

[Hab98] Richard Haberman. *Elementary applied partial differential equations : with Fourier series and boundary value problems.* Prentice Hall, Upper Saddle River, NJ, 3rd edition, 1998.

[Ham92] N. Hamada, S. Sawada, and A. Oshiyama. New one-dimensional conductors - graphitic microtubules. *Physical Review Letters*, 68(10):1579–1581, 1992.

[Han91] Chen Han-Taw and Lin Jae-Yuh. Hybrid laplace transform technique for non-linear transient thermal problems. *International Journal of Heat and Mass Transfer*, 34(4-5):1301–1308, 1991.

[Han06] Heine A. Hansen, Jakob L. Olsen, Soren Jensen, Ole Hansen, and Ulrich J. Quaade. Rate enhancement in microfabricated chemical reactors under fast forced temperature oscillations. *Catalysis Communications*, 7(5):272–275, 2006.

[Har05a] A.J. Hart and Slocum. A.H. Design and fabrication of microchannel arrays for combinatorial studies of nanomaterials growth,. In *Proceedings of the 5th International Conference of the European Society of Precision Engineering and Nanotechnology*, pages 81–84, Montpelier, France, 2005.

[Har05b] A.J. Hart and Slocum. A.H. Methods and devices for growth and/or assembly of nanostructures. u.s. utility patent application, 2005.

[Har05c] A.J. Hart, L.C. van Laake, and Slocum. A.H. Apparatus and methods for controlled growth and assembly of nanostructures. u.s. provisional patent application, 2005.

[Har06] A. J. Hart and A. H. Slocum. Rapid growth and flow-mediated nucleation of millimeter-scale aligned carbon nanotube structures from a thin-film catalyst. *J. Phys. Chem. B*, 110(16):8250–8257, 2006.

[Hel04] Stig Helveg, Carlos Lopez-Cartes, Jens Sehested, Poul L. Hansen, Bjerne S. Clausen, Jens R. Rostrup-Nielsen, Frank Abild-Pedersen, and Jens K. Norskov. Atomic-scale imaging of carbon nanofibre growth. *Nature*, 427(6973):426–429, 2004.

[Hof79] Douglas R. Hofstadter. *Gdel, Escher, Bach : an eternal golden braid.* Basic Books, New York, 1979.

[Hua03] S. Huang, Maynor B., Cai X., and Liu J. Ultralong, well-aligned single-walled carbon nanotube architectureson surfaces. *Advanced Materials*, 15(19):1651–1655, 2003.

[Hua04] S. M. Huang, M. Woodson, R. Smalley, and J. Liu. Growth mechanism of oriented long single walled carbon nanotubes using "fast-heating" chemical vapor deposition process. *Nano Letters*, 4(6):1025–1028, 2004.

[Hug89] T.V. Hughes and C.R. Chambers. United states patent no. 405480: Manufacture of carbon filaments, 1889.

[Iij80] Sumio Iijima. Direct observation of the tetrahedral bonding in graphitized carbon black by high resolution electron microscopy. *Journal of Crystal Growth*, 50(3):675–683, 1980.

[Iij91] S. Iijima. Helical microtubules of graphitic carbon. *Nature*, 354(6348):56–58, 1991.

[Iij93] Sumio Iijima and Toshinari Ichihashi. Single-shell carbon nanotubes of 1-nm diameter. *Nature*, 363(6430):603–605, 1993.

[Inc96] Frank P. Incropera and David P. DeWitt. *Introduction to heat transfer.* Wiley, New York, 3rd edition, 1996.

[inf] II-VI infrared. http://www.iiviinfrared.com/tutorials.html.

[Jai71] S. C. Jain, S. K. Agarwal, W. N. Borle, and S. Tata. Total emissivity of silicon at high temperatures. *Journal of Physics D: Applied Physics*, 4(8):1207–1209, 1971.

[Jan00] William S. Janna. *Engineering heat transfer.* CRC Press, Boca Raton, Fla., 2nd edition, 2000.

[Kro85] H. W. Kroto, J. R. Heath, S. C. Obrien, R. F. Curl, and R. E. Smalley. C-60 - buckminsterfullerene. *Nature*, 318(6042):162–163, 1985.

[Li04] Y. L. Li, I. A. Kinloch, M. S. P. Shaffer, C. Singh, J. F. Geng, B. F. G. Johnson, and A. H. Windle. Growth of single-walled carbon nanotubes by the rapid heating of a supported catalyst. *Chemistry of Materials*, 16(26):5637–5643, 2004.

[Lou03] Oleg A. Louchev, Thomas Laude, Yoichiro Sato, and Hisao Kanda. Diffusion-controlled kinetics of carbon nanotube forest growth by chemical vapor deposition. *The Journal of Chemical Physics*, 118(16):7622–7634, 2003.

[Mey05] M. Meyyappan. *Carbon nanotubes : science and applications.* CRC Press, Boca Raton, FL, 2005.

[Min92] J. W. Mintmire, B. I. Dunlap, and C. T. White. Are fullerene tubules metallic. *Physical Review Letters*, 68(5):631–634, 1992.

[Mor54] Maita J. P. Morin, F. J. Electrical properties of silicon containing arsenic and boron. *Physical Review*, 96(1):28–35, 1954.

[Nov04] K. S. Novoselov, A. K. Geim, S. V. Morozov, D. Jiang, Y. Zhang, S. V. Dubonos, I. V. Grigorieva, and A. A. Firsov. Electric field effect in atomically thin carbon films. *Science*, 306(5696):666–669, 2004.

[Obe76a] A. Oberlin, M. Endo, and T. Koyama. Filamentous growth of carbon through benzene decomposition. *Journal of Crystal Growth*, 32(3):335–349, 1976.

[Obe76b] A. Oberlin, M. Endo, and T. Koyama. High resolution electron microscope observations of graphitized carbon fibers. *Carbon*, 14(2):133–135, 1976.

[Pea49a] Bardeen J. Pearson, G. L. Electrical properties of pure silicon and silicon alloys containing boron and phosphorus. *Physical Review*, 75(5):865883, 1949.

[Pea49b] Bardeen J. Pearson, G. L. Erratum: Electrical properties of pure silicon and silicon alloys. *Physical Review*, 77(2):303, 1949.

[Rod93] N. M. Rodriguez, M. S. Kim, and R. T. K. Baker. Promotional effect of carbon monoxide on the decomposition of ethylene over an iron catalyst. *Journal of Catalysis*, 144(1):93–108, 1993.

[Sai92] R. Saito, M. Fujita, G. Dresselhaus, and M. S. Dresselhaus. Electronic-structure of graphene tubules based on c-60. *Physical Review B*, 46(3):1804–1811, 1992.

[Sel83] S. A. Self. Focusing of spherical gaussian beams. *Applied Optics*, 22(5):658–661, 1983.

[Sue04] O. Suekane, T. Nagasaka, K. Kiyotaki, T. Nosaka, and Y. Nakayama. Rapid growth of vertically aligned carbon nanotubes. *Japanese Journal of Applied Physics Part 2-Letters and Express Letters*, 43(9A-B):L1214–L1216, 2004.

[Sze02] S. M. Sze. *Semiconductor devices, physics and technology.* Wiley, New York, 2nd edition, 2002.

[Tho02] K. Thompson, Y. B. Gianchandani, J. Booske, and R. F. Cooper. Direct silicon-silicon bonding by electromagnetic induction heating. *Journal of Microelectromechanical Systems*, 11(4):285–292, 2002.

[Zen05] Z. Zeng and K. Natesan. Relationship between the growth of carbon nanofilaments and metal dusting corrosion. *Chemistry of Materials*, 17(14):3794–3801, 2005.

[Zhu05] Suenaga K. Hashimoto A. Urita K. Hata K. Iijima S. Zhu, H. Atomic-resolution imaging of the nucleation points of single-walled carbon nanotubes. *Small*, 1(12):1180–1183, 2005. 10.1002/smll.200500200.

Appendix A

Existing experiment protocols

A.1 Micro-channel device

1. atmospheric gas is displaced from the furnace by flushing with 400 sccm Ar for 10 minutes
2. tube furnace temperature is ramped to the setpoint in 30 minutes, while 400 sccm Ar is continued
    - Ar is at the same time flowing backwards through the channels at 0.25 psi pressure drop
    - setpoint typically 750°C for MWNT growth in C_2H_4
    - setpoint typically 850°C for SWNT growth in CH_4)
3. Ar is continued for another 25 minutes while the furnace temperature stabilizes
4. H_2/Ar is introduced into the furnace for 5 minutes
5. for the last 1 minute of H_2/Ar, the flow through the channels is reversed by switching the three-way valve. Gas from the tube furnace is now drawn into the micro-channels by the under-pressure.
6. reaction species are introduced for the duration of the experiment
    - typically 5 -15 minutes
    - C_2H_4/H_2/Ar for MWNT growth
    - H_2/CH_4 for SWNT growth
7. 400 sccm Ar is introduced into the tube furnace, and the furnace is turned off and opened to cool.
    - for the first 5 minutes, flow into channels is maintained by underpressure, then vacuum generator turned off.

A.2 Regular substrate

1. atmospheric gas is displaced from the furnace by flushing with 400 sccm Ar for 10 minutes
2. temperature of the furnace is ramped to the setpoint in 30 minutes, while 400 sccm Ar is continued
   - typically 750°C for MWNT growth in C_2H_4
   - typically 850°C for SWNT growth in CH_4)
3. 400 sccm Ar is continued for another 15 minutes while the furnace temperature stabilizes
4. reaction species are introduced for the duration of the experiment
   - H_2 is introduced 1 – 5 minutes before carbon feedstock
   - typically 15 minutes, but times up to over 60 minutes have been studied
   - typically 100/500/200 sccm $C_2H_4/H_2/Ar$ for MWNT growth
   - typically 40/350 sccm H_2/CH_4 for SWNT growth
5. furnace is turned off and opened to cool

Appendix B

Implementation of thermal model in Matlab

B.1 heatermain.m

```
heatermain.m by:

clear all

global t_o P_kSB P_CSB P_kHH P_CHH Pnus eps_SB rho_SB...
    eps_HH rho_HH pars dims_SB dims_HH lookup_res_HH tdata Idata

% from propertiesfinal.m:
load propsfit
load Pnusfit

eps_SB = 0.5;
rho_SB = 7900;

eps_HH = 0.65;
rho_HH = 2330;

T1=1150:10:1300;
rhointr=10.^(-4.2953+2947.8./T1)/100;
T3=  [300     400     500     600     700     800     825...
    850     875     900     925     950     1000    1050];
rho3=[0.0240 0.0264 0.0292 0.033  0.0385 0.0455 0.0465...
    0.047 0.0465 0.045  0.0435 0.041  0.0360 0.03]/100;
```

```
T3=  [300     400     500     600     700     800     825     ...
    850     875    900     925     950     1000    1050];
rho3=[0.0240 0.0264 0.0292 0.033  0.0375 0.0435 0.045...
    0.0455 0.045 0.0435 0.041 0.038  0.0330 0.028]/100;

res_Si_u=[T3,T1]';
res_Si_res=[rho3,rhointr]';

lookup_res_HH=[res_Si_u,res_Si_res];

%parameters
u_inf=298;
R_therm=9;
sig=5.67e-8;

pars=[u_inf;R_therm;sig];

W_SB=20/1000;
H_SB=10/1000;
x_SB=40/1000;
S_SB = 2*(W_SB+H_SB)*x_SB;
A_SB=W_SB*H_SB;
V_SB=A_SB*x_SB;

W_HH=10/1000;
H_HH=0.3/1000;
x_HH=x_SB+42.5/1000;
S_HH = 2*(W_HH+H_HH)*(x_HH-x_SB);
A_HH=W_HH*H_HH;
A_resHH=A_HH;
V_HH=A_HH*(x_HH-x_SB);

dims_SB = [S_SB; A_SB; V_SB; x_SB];
dims_HH = [S_HH; A_HH; V_HH; A_resHH; x_HH];

%evaluate material props at u_bar, for scaling factors
T(1)=700;
T(2)=900;
Tsca=(T-u_inf)/u_inf;

k_SB   = polyval(P_kSB,T(1));
C_SB   = polyval(P_CSB,T(1));
```

```
invers = inline('P(1)./T.^2 + P(2)./T','P','T');
k_HH   = invers(P_kHH,T(2));
squro = inline('P(1).*(T+P(2)).^P(3)','P','T');
C_HH   = squro(P_CHH,T(2));

nusfunc = inline('P(1)-P(2).*exp(-T/P(3))','P','T');
h_SB=nusfunc(Pnus,T(1));
h_HH=nusfunc(Pnus,T(2));


%calculate scaled factors
t_dSB = rho_SB*C_SB*V_SB* (x_SB)/(k_SB*A_SB);
t_cSB = rho_SB*C_SB*V_SB* 1/(h_SB*S_SB);
t_rSB = rho_SB*C_SB*V_SB* Tsca(1)/(sig*eps_SB*u_inf^3*S_SB...
    *((Tsca(1)+1)^4-1));
Fo_SB = (k_SB*t_dSB)/(x_SB^2*rho_SB*C_SB);

t_dHH = rho_HH*C_HH*V_HH* (x_HH-x_SB)/(k_HH*A_HH);
t_cHH = rho_HH*C_HH*V_HH* 1/(h_HH*S_HH);
t_rHH = rho_HH*C_HH*V_HH* Tsca(2)/(sig*eps_HH*u_inf^3...
    *S_HH*((Tsca(2)+1)^4-1));
Fo_HH = (k_HH*t_dHH)/((x_HH-x_SB)^2*rho_HH*C_HH);

t_o   = 1/(1/t_cHH+1/t_rHH+1/(t_dHH+t_dSB+1/(1/t_cSB+...
    1/t_rSB)));

% scaled calculation grid 0:1
x_=[0 0.1 0.2 0.3 0.5 0.65 0.8 0.85 0.9 0.95 0.975 1];

%measured data
datafile='profiling3.txt';SR=2; %data sample rate

%run scaledheater.m
[t_,sol_,calctime,dataset]=scaledheater(datafile,x_,SR);

%plot settings
plots{1}=1;
plots{2}=10:10:500;
plots{3}=0;

%postprocess
postproc;
```

B.2 scaledheater.m

```
substrateheater.m

function [t_,sol_,calctime,dataset]=scaledheater(datafile,x_,SR)

substrateheater.m

global t_o tdata Idata;

data=load(datafile);
load irTCfitpars;
TirTCfit=[0:1000];
VirTCfit=polyval(PirTC,TirTCfit);

T1=[0;data(:,1)];
T2=[0;data(:,2)];
T3=[0;data(:,3)];
T4=[0;data(:,4)];
T5=[0;data(:,5)];
TIR=[0;interp1(VirTCfit,TirTCfit,data(:,6),'linear');];

Idata=[0;data(:,7)];
Vdata=[0;data(:,8)];
Rdata=Vdata./Idata;

tdata=[0,(1:length(T1)-1)/SR]'; % sample frequency SR Hz
tend=tdata(end);
t=linspace(0,tend,500); % t where solution is given (calculation...
    is refined until convergence: not influenced by this t vector)

t_=t./t_o;

dataset=[T1,T2,T3,T4,T5,TIR,Vdata,Rdata];

clear T1 T2 T3 T4 T5 TIR Vdata Rdata tend

m = 0;

OPTIONS = ODESET('reltol',1e-4);

tic;
sol_ = pdepe(m,@heatpde,@heatic,@heatbc,x_,t_,OPTIONS);
```

```
calctime=toc;

% ------------------------------------------------------

function [c,f,s] = heatpde(x,t,u,DuDx);

global t_o P_kSB P_CSB P_kHH P_CHH Pnus eps_SB rho_SB eps_HH...
    rho_HH pars dims_SB dims_HH tdata Idata lookup_res_HH;

u_inf = pars(1);
sig=pars(3);

S_SB = dims_SB(1);
A_SB = dims_SB(2);
V_SB = dims_SB(3);
x_SB = dims_SB(4);

S_HH = dims_HH(1);
A_HH = dims_HH(2);
V_HH = dims_HH(3);
A_resHH = dims_HH(4);
x_HH = dims_HH(5);

%unscale time and temp
t=t*t_o;
T=u*u_inf+u_inf;

k_SB   = polyval(P_kSB,T(1));
C_SB   = polyval(P_CSB,T(1));

invers = inline('P(1)./T.^2 + P(2)./T','P','T');
k_HH   = invers(P_kHH,T(2));
squro = inline('P(1).*(T+P(2)).^P(3)','P','T');
C_HH   = squro(P_CHH,T(2));

nusfunc = inline('P(1)-P(2).*exp(-T/P(3))','P','T');
h_SB=nusfunc(Pnus,T(1));
h_HH=nusfunc(Pnus,T(2));

%calculate scaled factors
t_dSB = rho_SB*C_SB*V_SB* (x_SB)/(k_SB*A_SB);
t_cSB = rho_SB*C_SB*V_SB* 1/(h_SB*S_SB);
t_rSB = rho_SB*C_SB*V_SB* u(1)/(sig*eps_SB*u_inf^3*S_SB*...
    ((u(1)+1)^4-1));
```

```
Fo_SB = (k_SB*t_dSB)/(x_SB^2*rho_SB*C_SB);

t_dHH = rho_HH*C_HH*V_HH* (x_HH-x_SB)/(k_HH*A_HH);
t_cHH = rho_HH*C_HH*V_HH* 1/(h_HH*S_HH);
t_rHH = rho_HH*C_HH*V_HH* u(2)/(sig*eps_HH*u_inf^3*S_HH*...
    ((u(2)+1)^4-1));
Fo_HH = (k_HH*t_dHH)/((x_HH-x_SB)^2*rho_HH*C_HH);

QQ = (rho_HH*C_HH*u_inf)/t_o;

res_HH=interp1(lookup_res_HH(:,1),lookup_res_HH(:,2),...
    T(2),'linear');
I=interp1(tdata,Idata,t,'linear');
Q=I^2*res_HH/(A_resHH*A_HH); %Q=I^2*res/A^2 (from the...
     integral form of energy conservation)
Q_=Q/QQ;

f1 = Fo_SB*t_o/t_dSB*DuDx(1);
f2 = Fo_HH*t_o/t_dHH*DuDx(2);
s1 = - (t_o/t_cSB+t_o/t_rSB)*u(1);
s2 = - (t_o/t_cHH+t_o/t_rHH)*u(2) + Q_;

c = [1;1];
f=[f1;f2];
s=[s1;s2];

% ---------------------------------------------------

function u0 = heatic(x)

u0 = [0.01;0.01];

% ----------------------------------------------------
function [pzero,qzero,pone,qone] = heatbc(xzero,uzero,..
    xone,uone,t)

global t_o P_kSB P_CSB P_kHH P_CHH Pnus eps_SB rho_SB eps_HH..
     rho_HH dims_SB dims_HH pars

u_inf=pars(1);
R_therm=pars(2);
sig=pars(3);

S_SB = dims_SB(1);
```

```
A_SB = dims_SB(2);
V_SB = dims_SB(3);
x_SB = dims_SB(4);

S_HH = dims_HH(1);
A_HH = dims_HH(2);
V_HH = dims_HH(3);
A_resHH = dims_HH(4);
x_HH = dims_HH(5);

Tzero=uzero*u_inf+u_inf;
Tone=uone*u_inf+u_inf;

nusfunc = inline('P(1)-P(2).*exp(-T/P(3))','P','T');
h_SBzero  =nusfunc(Pnus,Tzero(1));
h_SBone   =nusfunc(Pnus,Tone(1));
h_HHzero  =nusfunc(Pnus,Tzero(2));
h_HHone   =nusfunc(Pnus,Tone(2));

k_SBzero   = polyval(P_kSB,Tzero(1));
C_SBzero   = polyval(P_CSB,Tzero(1));
k_SBone   = polyval(P_kSB,Tone(1));
C_SBone   = polyval(P_CSB,Tone(1));
rho_SB = 7900;

invers = inline('P(1)./T.^2 + P(2)./T','P','T');
squro = inline('P(1).*(T+P(2)).^P(3)','P','T');
k_HHzero   = invers(P_kHH,Tzero(2));
C_HHzero   = squro(P_CHH,Tzero(2));
k_HHone   = invers(P_kHH,Tone(2));
C_HHone   = squro(P_CHH,Tone(2));
rho_HH = 2330;

t_dSBzero = rho_SB*C_SBzero*V_SB* (x_SB)/(k_SBzero*A_SB);
t_cSBzero = rho_SB*C_SBzero*V_SB* 1/(h_SBzero*S_SB);
t_rSBzero = rho_SB*C_SBzero*V_SB* uzero(1)/(sig*eps_SB*..
    u_inf^3*S_SB*((uzero(1)+1)^4-1));
Fo_SBzero = (k_SBzero*t_dSBzero)/(x_SB^2*rho_SB*C_SBzero);

t_dSBone = rho_SB*C_SBone*V_SB* (x_SB)/(k_SBone*A_SB);
t_cSBone = rho_SB*C_SBone*V_SB* 1/(h_SBone*S_SB);
t_rSBone = rho_SB*C_SBone*V_SB* uone(1)/(sig*eps_SB*u_inf^3..
    *S_SB*((uone(1)+1)^4-1));
Fo_SBone = (k_SBone*t_dSBone)/(x_SB^2*rho_SB*C_SBone);
```

```
t_dHHzero = rho_HH*C_HHzero*V_HH* (x_HH-x_SB)/(k_HHzero*A_HH);
t_cHHzero = rho_HH*C_HHzero*V_HH* 1/(h_HHzero*S_HH);
t_rHHzero = rho_HH*C_HHzero*V_HH* uzero(2)/(sig*eps_HH*..
    u_inf^3*S_HH*((uzero(2)+1)^4-1));
Fo_HHzero = (k_HHzero*t_dHHzero)/((x_HH-x_SB)^2*rho_HH..
    *C_HHzero);

t_dHHone = rho_HH*C_HHone*V_HH* (x_HH-x_SB)/(k_HHone..
    *A_HH);
t_cHHone = rho_HH*C_HHone*V_HH* 1/(h_HHone*S_HH);
t_rHHone = rho_HH*C_HHone*V_HH* uone(2)/(sig*eps_HH*...
    u_inf^3*S_HH*((uone(2)+1)^4-1));
Fo_HHone = (k_HHone*t_dHHone)/((x_HH-x_SB)^2*rho_HH..
    *C_HHone);

%calculate scaled factors
RR_SB = x_SB/(k_SBone*A_SB)*(t_o/t_dSBone);
RR_HH = (x_HH-x_SB)/(k_HHone*A_HH)*(t_o/t_dHHone);
R_SB = R_therm/RR_SB;
R_HH = R_therm/RR_HH;

pzero1 = -A_SB/S_SB*(t_o/t_cSBzero + t_o/t_rSBzero)..
    *uzero(1);
qzero1 = 1;
pzero2 = 0;
qzero2 = 1;

pzero = [pzero1;pzero2];
qzero = [qzero1;qzero2];

pone = [1/R_SB*(uone(2)-uone(1));-1/R_HH*(uone(2)..
    -uone(1))];
qone = -[1/Fo_SBone;1/Fo_HHone];
```

Appendix C

Calculation of Nusselt numbers

```
Nusselt.m

T=300:200:1100;
Tf=(300+T)/2;
nu=[15.89,26.41,38.79,52.69,68.1]*1e-6;
alfa=[22.5,38.3,56.7,76.9,98]*1e-6;
Pr=[0.71,0.69,0.684,0.685,0.695];
beta=1./T;
k=[0.0263000,0.0338000,0.0407000,0.0469000,0.0524000];

g=9.81;

v=0.01; \%v=0.001/pi/0.025^2/60 = 0.008
Lnat=0.005;
Lforc=0.05;

Re=Lforc*v./nu;
Ra=g.*beta.*(T-298)*Lnat^3./nu./alfa;
\%Ra =    22.8655  489.7712  320.1874  202.4317  133.9638

Nu_up=0.54*Ra.^(1/4);
Nu_down=0.27*Ra.^(1/4);
Nu_forc=0.664*Pr.^(1/2).*Re.^(1/2);
figure;plot(T,[Nu_up;Nu_down;Nu_forc])

h_up=Nu_up.*k/Lnat;
h_down=Nu_down.*k/Lnat;
h_forc=Nu_forc.*k/Lforc;
figure;plot(T,[h_up;h_down;h_forc])
```

Using from [Jan00]:

Heated plate, facing upward (natural convection)

$$Nu = \frac{hL}{k_f} = 0.54\mathrm{Ra}^{1/4},\ 2.6 \times 10^4 < \mathrm{Ra} < 3 \times 10^7 \tag{C.1}$$

Heated plate, facing downward (natural convection)

$$Nu = 0.27\mathrm{Ra}^{1/4},\ 3 \times 10^5 < \mathrm{Ra} < 3 \times 10^{1}0 \tag{C.2}$$

Heated plate (forced convection)

$$Nu = 0.664\mathrm{Pr}^{1/2}\mathrm{Re}^{1/2},\ Re < 5 \times 10^5 \tag{C.3}$$

where

Nu	average Nusselt number [–]]
h	average convection heat transfer coefficient [W/(m^2 K)]
L	characteristic length [m]
k_f	thermal conductivity of fluid [W/(m K)], evaluated at film temperature $T_f = \frac{T+T_\infty}{2}$
Ra	Rayleigh number = $\frac{g\beta(T-T_\infty)L^3}{\nu\alpha}$ [–]
β	inverse temperature [1/K]
ν	kinematic viscosity [m^2/s]
α	thermal diffusivity [m^2/s]
Pr	Prandtl number [–]
Re	Reynolds number = $\frac{vL}{nu}$ [–]
v	fluid velocity [m/s]

Material properties of Ar from [Inc96]

The conditions for applicability of the free-convection approximations is not met, since $Ra \sim 100$. The general form by which transfer increases with temperature is assumed to be correct, and it is approximated by an exponential function for faster numerical integration:

$$h = P_1 - P_2 e^{-T/P_3} \tag{C.4}$$

and least-squares fitting parameters are found using `nlinfit.m`.

$$P = [19.1285208.6475107.8185]$$

Theses values result from a fit to the values for a plate facing upward. This results in a good match with measured data. The fitted $h(T)$ is depicted in Fig. C.1 along with the calculated values for the forced and natural convection approximations.

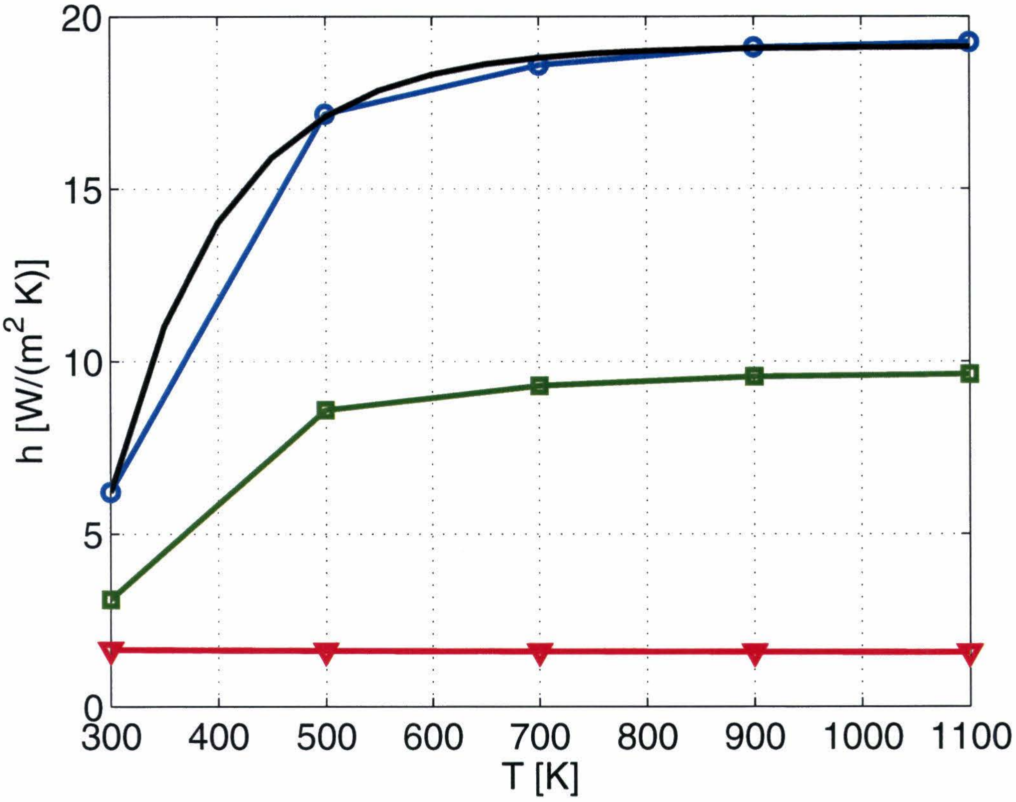

Figure C.1: Convection heat transfer coefficients and non-linear fit

Appendix D

Clam-shell design

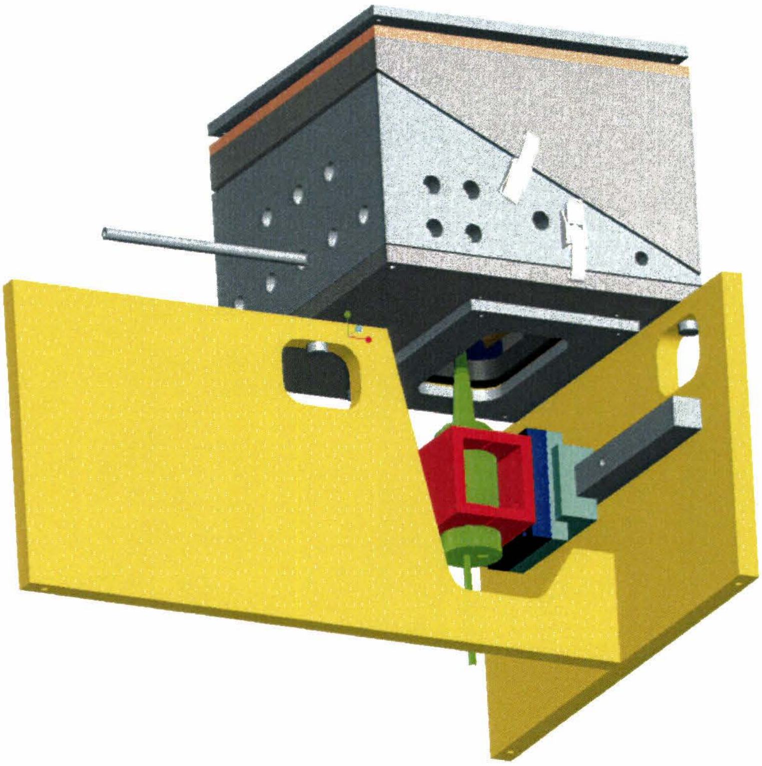

Figure D.1: Clam-shell design, including stand and IR thermopile sensor mounted to a linear bearing